



**Calhoun: The NPS Institutional Archive**  
**DSpace Repository**

---

Theses and Dissertations

1. Thesis and Dissertation Collection, all items

---

1992-09

Analysis of a simulation of the seasonal cycle  
in the tropical Pacific Ocean in an  
eddy-resolving global ocean model.

Gordon, Lawrence Joseph

Monterey, California. Naval Postgraduate School

---

<http://hdl.handle.net/10945/23537>

---

*Downloaded from NPS Archive: Calhoun*



Calhoun is the Naval Postgraduate School's public access digital repository for research materials and institutional publications created by the NPS community. Calhoun is named for Professor of Mathematics Guy K. Calhoun, NPS's first appointed -- and published -- scholarly author.

**Dudley Knox Library / Naval Postgraduate School**  
**411 Dyer Road / 1 University Circle**  
**Monterey, California USA 93943**

<http://www.nps.edu/library>





DUDLEY FOX LIBRARY  
NAVA: GRADUATE SCHOOL  
MONTEREY CA 93943-5101





Unclassified

Security Classification of this page

## REPORT DOCUMENTATION PAGE

1a Report Security Classification <b>Unclassified</b>		1b Restrictive Markings	
2a Security Classification Authority		3 Distribution Availability of Report	
2b Declassification/Downgrading Schedule		Approved for public release; distribution is unlimited.	
4 Performing Organization Report Number(s)		5 Monitoring Organization Report Number(s)	
6a Name of Performing Organization <b>Naval Postgraduate School</b>	6b Office Symbol (If Applicable) <b>OC</b>	7a Name of Monitoring Organization <b>Naval Postgraduate School</b>	
6c Address (city, state, and ZIP code) <b>Monterey, CA 93943-5000</b>		7b Address (city, state, and ZIP code) <b>Monterey, CA 93943-5000</b>	
8a Name of Funding/Sponsoring Organization	8b Office Symbol (If Applicable)	9 Procurement Instrument Identification Number	
8c Address (city, state, and ZIP code)		10 Source of Funding Numbers	
		Program Element Number	Project No
		Task No	Work Unit Accession No
11 Title (Include Security Classification) <b>ANALYSIS OF A SIMULATION OF THE SEASONAL CYCLE IN THE TROPICAL PACIFIC OCEAN IN AN EDDY-RESOLVING GLOBAL OCEAN MODEL</b>			
12 Personal Author(s) <b>Gordon, Lawrence J.</b>			
13a Type of Report <b>Master's Thesis</b>	13b Time Covered From To	14 Date of Report (year, month, day) <b>September 1992</b>	15 Page Count <b>82</b>
16 Supplementary Notation <b>The views expressed in this thesis are those of the author and do not reflect the official policy or position of the Department of Defense or the U.S. Government.</b>			
17 Cosati Codes		18 Subject Terms (continue on reverse if necessary and identify by block number)	
Field	Group	Subgroup	
		Oceanographic Numerical Modeling, Pacific Ocean, Ocean General Circulation Model, Eddy-Resolving, Tropical, Equatorial Currents	
19 Abstract (continue on reverse if necessary and identify by block number)			
<p>This paper examines the multi-level, primitive equation, global ocean circulation model of Semtner and Chervin for its ability to simulate the seasonal cycle in the tropical Pacific Ocean. The result of a 20-year integration of this model using annual mean wind forcing was reported in Semtner and Chervin (1988). This was the first global eddy-resolving ocean calculation and it showed many realistic features of ocean circulation. The phase of the simulation analyzed in this report incorporates seasonally varying wind forcing from the Hellerman and Rosenstein (1983) global data set. These wind stress values were defined on a grid with 2° spacing which have been interpolated to the one-half degree grid points of the Semtner and Chervin model. There is no interannual variability in the wind fields of this data set. The results presented here are from the fourth year of a 10-year seasonal cycle run.</p> <p>The upper oceanic circulation of the equatorial Pacific Ocean consists of alternating westward and eastward flows that vary seasonally in strength and extent. The eastward flows investigated in this study are the Equatorial Undercurrent and North Equatorial Countercurrent; the westward currents are the North and South Equatorial Currents. The Equatorial Undercurrent is most intense late in the Northern Hemisphere spring and is weak in the late fall at which time the North Equatorial Countercurrent and the South Equatorial Current are most intense. This result is in agreement with observations and other model studies.</p>			
20 Distribution/Availability of Abstract <input checked="" type="checkbox"/> unclassified/unlimited <input type="checkbox"/> same as report <input type="checkbox"/> DTIC users		21 Abstract Security Classification <b>Unclassified</b>	
22a Name of Responsible Individual <b>Albert J. Semtner, Jr</b>		22b Telephone (Include Area Code) <b>(408) 646-3267</b>	22c Office Symbol <b>OC/Se</b>

DD FORM 1473, 84 MAR

83 APR edition may be used until exhausted

security classification of this page

All other editions are obsolete

Unclassified

T260442

Approved for public release; distribution is unlimited.

Analysis of a Simulation of the Seasonal  
Cycle in the Tropical Pacific Ocean  
in an Eddy-Resolving Global Ocean Model

by

Lawrence Joseph Gordon  
Lieutenant Commander, United States Navy  
B.S., Tulane University, 1981

Submitted in partial fulfillment  
of the requirements for the degree of

MASTER OF SCIENCE IN METEOROLOGY AND  
PHYSICAL OCEANOGRAPHY

from the

NAVAL POSTGRADUATE SCHOOL

September 1992

---

## ABSTRACT

This paper examines the multi-level, primitive equation, global ocean circulation model of Semtner and Chervin for its ability to simulate the seasonal cycle in the tropical Pacific Ocean. The result of a 20-year integration of this model using annual mean wind forcing was reported in Semtner and Chervin (1988). This was the first global eddy-resolving ocean calculation and it showed many realistic features of ocean circulation. The phase of the simulation analyzed in this report incorporates seasonally varying wind forcing from the Hellerman and Rosenstein (1983) global data set. These wind stress values were defined on a grid with  $2^\circ$  spacing which have been interpolated to the one-half degree grid points of the Semtner and Chervin model. There is no interannual variability in the wind fields of this data set. The results presented here are from the fourth year of a 10-year seasonal cycle run.

The upper oceanic circulation of the equatorial Pacific Ocean consists of alternating westward and eastward flows that vary seasonally in strength and extent. The eastward flows investigated in this study are the Equatorial Undercurrent and North Equatorial Countercurrent; the westward currents are the North and South Equatorial Currents. The Equatorial Undercurrent is most intense late in the Northern Hemisphere spring and is weak in the late fall at which time the North Equatorial Countercurrent and the South Equatorial Current are most intense. This result is in agreement with observations and other model studies.



201

## TABLE OF CONTENTS

I. INTRODUCTION . . . . .	1
A. BACKGROUND . . . . .	1
B. PACIFIC OCEAN . . . . .	3
II. GLOBAL OCEAN MODEL . . . . .	5
A. MODEL PARAMETERS . . . . .	5
B. MONTHLY MEAN WIND STRESS . . . . .	7
III. RESULTS AND DISCUSSION . . . . .	13
A. EDDY-RESOLVING NATURE OF THE GLOBAL MODEL . . . . .	13
B. MEAN ANNUAL STRUCTURE IN THE CENTRAL PACIFIC . . . . .	18
C. SEASONAL CYCLE IN THE EQUATORIAL PACIFIC . . . . .	26
D. WESTERN EQUATORIAL PACIFIC . . . . .	29
IV. CONCLUSIONS AND RECOMMENDATIONS . . . . .	31
APPENDIX (FIGURES) . . . . .	33

LIST OF REFERENCES .....	71
--------------------------	----

INITIAL DISTRIBUTION LIST .....	73
---------------------------------	----



## I. INTRODUCTION

### A. BACKGROUND

Ocean numerical modelers for many years have been limited in the scope of the ocean model studies they can achieve because of limitations in computer power and resources. Oceanographers have watched numerical modeling in the meteorology community grow into a critical tool for understanding and predicting the weather. In contrast to atmospheric modeling, world ocean "climate" modeling requires a thousand-fold increase in computer power due to the order of magnitude increase in each horizontal direction required to model oceanic features versus atmospheric (because the Rossby radius of deformation at midlatitudes is typically 400 km in the atmosphere and 40 km in the ocean). Integration time for numerical ocean models requires another ten-fold increase due to the longer time scales of oceanic phenomenon. Oceanographers also suffer from a paucity of observational data with which to initialize models. Because of these factors, oceanographers have lagged behind their colleagues in meteorology in many phases of applications, research with and prognostic use of numerical modeling.

Modern generations of supercomputers are finally available to oceanographers that are powerful enough to run "full physics" general circulation simulations on a global scale. Still the resolution of these ocean general circulation models are marginal in their ability to resolve mesoscale eddies, the oceanic equivalent of atmospheric cyclones and anticyclones. A computer simulation of the tropical oceans holds the most promise in



having "realistic" currents and thermal structure from a marginal eddy-resolving global ocean model because of the larger Rossby radius of deformation ( $\sim 140$  km) near the equator. This paper is an analysis of the results in the tropical Pacific Ocean of one such global simulation.

In recent years, a large amount of public attention has been focused on the question of "global warming." The growing global environmental movement owes its popularity in large part to public perceptions and concerns for this issue. Vast sums of research dollars are being funneled into investigating climate change. Scientists have long known that the earth undergoes natural climate change over long periods. The question is whether or not human activities since the industrial revolution have accelerated climate change, change which may have unforeseen and possibly catastrophic consequences for much of the world's population in the form of starvation, social and political upheaval.

The ocean is known to be a sink for carbon dioxide and can store and redistribute a vast amount of heat. The tropical oceans play a critical but poorly understood role in this redistribution of heat. The feedback between the atmosphere and the ocean will require the most sophisticated coupled ocean-atmosphere models in order to accurately simulate climate variability.

Scientists cannot hope to have an accurate coupled ocean-atmosphere model for studies of long-term climate change until we first have an understanding and can model oceanic heat flux and global ocean circulation. The Semtner and Chervin global circulation model, hereafter referred to as the SC-GCM, is an attempt to model the global ocean circulation.

The SC-GCM, is a one-half degree primitive equation model that ran for a 20-year integration using annual mean wind forcing. This simulation showed many realistic features of oceanic circulation (Semtner and Chervin, 1988). The next step in the evolution of this model was to incorporate seasonally varying forcing of wind from the Hellerman and Rosenstein (1983) global data set and seasonal heat and salt fluxes from the Levitus (1982) data base. Assuming the forcing is reasonably correct, the simulation should produce a strong seasonal cycle in the tropical oceans. The results of the model presented are from the fourth year of a 10-year seasonal cycle run.

## **B. PACIFIC OCEAN**

The upper oceanic circulation of the equatorial Pacific Ocean consists of alternating westward and eastward flows as shown schematically in Figure 1.1. The four major currents consist of three surface currents, the westward flowing North Equatorial Current (NEC) extending between latitudes  $10^{\circ}\text{N}$  and  $20^{\circ}\text{N}$ , the westward flowing South Equatorial Current (SEC) between  $3^{\circ}\text{N}$  and  $10^{\circ}\text{S}$ , and between these two westward surface currents, the eastward flowing North Equatorial Countercurrent (NECC). The Equatorial Undercurrent (EUC) is the fourth major current and is a submerged current flowing eastward along the equator from  $2^{\circ}\text{N}$  to  $2^{\circ}\text{S}$ . Observationalists have documented that the Equatorial Undercurrent is most intense during the Northern Hemisphere spring and is weak in the fall at which time the North Equatorial Countercurrent and the South Equatorial Current are most intense. The existence of these four currents has been known for many years, but scientists are still far from a comprehensive understanding

of their variability both seasonally and interannually. Oceanographers know in a qualitative sense that these currents vary seasonally and spatially in strength and vertical and horizontal extent, *i.e.*, volume transport. They have no clear understanding of their climatological state on an annual and seasonal basis. Because of the large interannual variability in the forcing over the tropical Pacific Ocean, such a climatology would require observations over many years and over a huge expanse of ocean. General circulation numerical ocean models are important tools in assisting oceanographers to arrive at this understanding.

The organization of this thesis is as follows. A brief description of the model used occurs in Chapter II, along with the trade wind system which drives the surface currents in the tropics. Next, the major equatorial currents in the model are examined in the model and compared to observational studies. Additionally, the seasonal variations of these currents and the associated variation of wind forcing are examined (Chapter III). Several lesser known off-equatorial currents are also resolved in the SC-GCM and are discussed. Finally, conclusions and recommendations are presented in Chapter IV.

## II. GLOBAL OCEAN MODEL

The model used in this study is the multi-level, primitive equation, robust-diagnostic global ocean circulation model of Semtner and Chervin (1988). This model has been described in detail in the existing oceanographic literature. What follows then is a general description of the global ocean model with the exception that the monthly varying wind stress field in the Pacific basin used in the model calculation will be discussed thoroughly. For the interested reader additional information on the SC-GCM formulation can found in Semtner (1986 a,b).

### A. MODEL PARAMETERS

The domain of the SC-GCM is all longitudes from latitudes 75°S to 65°N. The grid spacing is 1/2° degree in the horizontal and there are 20 levels in the vertical. Realistic coasts and bathymetry (slightly smoothed) are used.

Wind stress is specified from Hellerman and Rosenstein (1983)'s monthly averaged climatological analysis of ship winds. This global data set defines values on a grid of 2° spacing. For use in the 1/2° spacing of the SC-GCM, the wind data have been interpolated to the grid points of the model. A smooth transition curve was applied to the mean monthly values of wind stress from one month to the next to avoid "jolting" the model with sudden and unrealistic climatological changes. It should be emphasized that at this stage of the simulation, the wind stress used has seasonal but no interannual



variability. Thus the SC-GCM is not designed to model interannual phenomenon in the Pacific Ocean such as the El Niño/Southern Oscillation (ENSO).

Vertical mixing in the model uses the Richardson-number dependent parameterization of Pacanowski and Philander (1981). Effects of eddies smaller than the eddies resolved by the model are parameterized by biharmonic mixing. The SC-GCM is initialized with temperature and salinity values from the Levitus (1982) global data base. The upper 25 meters of the water column in the model are forced to these Levitus values on a monthly time scale in the method of Haney (1971). This serves as a proxy for heat and moisture fluxes. Below 700 meters temperature and salinity values are restored to Levitus data on a three-year time scale. Restoring within the thermocline (25-700 m) occurs only in latitude bands  $65^{\circ}\text{S}$ - $75^{\circ}\text{S}$  and  $55^{\circ}\text{N}$ - $65^{\circ}\text{N}$ , also on a three-year time scale. In all other latitude bands, including the Pacific equatorial region of this study, the thermocline is unconstrained and free to resolve its own temperature and salinity structure, currents and eddies. The model runs with a 900 second time step between iterations.

The model geometry has been simplified somewhat by connecting most major islands to continental land masses and shoaling remaining islands to a depth of 100 meters. For the Pacific portion of the global model (Figure 2.1), New Guinea is connected to Australia and the western Pacific islands of Celebes, Mindanao and Halmahera are submerged. Borneo and much of the Philippines are joined to the East Asian land mass and the marginal seas in between are filled in. All other islands in the Pacific are submerged with the exception of New Zealand. As will be shown in the

analysis of the results, this simplified geometry and bathymetry in the western Pacific has a significant impact on the model results for this area. Bathymetry in the model is determined by the number of vertical grid boxes at each location up to the limit of 20 (maximum model depth of 5200 meters). The boxes are stacked from the surface down until the local bottom is reached at each horizontal grid point. The 20 vertical grid levels have varying thicknesses to allow concentration of boxes in the upper portion of the ocean for enhanced thermocline resolution. The bathymetry of the model in the Pacific is shown in detail and at various depths in Figure 2.2.

The SC-GCM has completed 32.5 years of simulation with the first 22.5 years using annual mean wind forcing, heat and salt fluxes. Results from the annual mean run were discussed in Semtner and Chervin (1988). Monthly mean forcing has been run for the remaining 10 years. At the end of each three-day period of simulation, a "snapshot" was taken of the global ocean. Years 20-30 of the simulation are archived at these three-day intervals for ongoing analysis.

## **B. MONTHLY MEAN WIND STRESS**

The equatorial currents in the Pacific are driven by the trade wind system that persists throughout the year. The variations in the wind stress pattern cause variations in the position of the Intertropical Convergence Zone (ITCZ), the area between the northern and southern hemispheric trade wind belts where their convergence occurs. The seasonal variation in the wind stress field does not rival the monsoonal reversal seen in the Indian Ocean, but some monsoonal effects are present in the western Pacific Ocean.

Because the surface currents are wind-driven, an understanding of the major currents of the equatorial Pacific requires an understanding of the equatorial wind field. Figures 2.3-2.14 are vector diagrams of the annual cycle of wind stress in the equatorial Pacific Ocean from the Hellerman and Rosenstein (1983) global data set. The wind stress pattern will be described for the western and central equatorial Pacific first, then for the simpler pattern of the eastern Pacific.

In January (Figure 2.3a), strong northeasterly wind flow is prevalent in the central and western Pacific from the atmospheric pressure gradient around the Asiatic high. The northeasterly flow extends to the equator in the central Pacific. In the western Pacific the wind field is more complicated as it becomes northerly and even northwesterly as it turns along the Philippines and New Guinea coast. The southeasterly (SE) trades are weak and are evident along the 18-20°S latitudinal band. The ITCZ is the broad and diffuse area of weak winds along 10°S in the western Pacific and extending from the equator to approximately 16°S in the central Pacific. The northeasterly (NE) trades are at their strongest during this month with maximum wind stress values of approximately  $1.9 \text{ dyn cm}^{-2}$  in the Philippine Sea. The southeast trades are much weaker, with maximum values of  $0.9 \text{ dyn cm}^{-2}$  near the northeastern coast of Australia. The SE trades weaken toward the east.

The February wind pattern (Figure 2.3b) is little changed from January. The northeast monsoon and its associated winds have weakened slightly.

The azimuthal pattern of wind stress in March (Figure 2.4a) is nearly identical to the first two months except that the northeast monsoon has weakened with wind stress

values of  $1.2 \text{ dyn cm}^{-2}$  in the western equatorial Pacific. The southeast trades have increased in strength, but they remain as a broad area of weak winds extending from the equator southward.

In April (Figure 2.4b), there is a pronounced weakening of the NE trades beginning in the western Pacific Ocean as the Asiatic high breaks down. Wind stress values are a maximum of  $0.7\text{-}0.8 \text{ dyn cm}^{-2}$ . In the central Pacific the NE trades have weakened only slightly. The SE trade winds have now increased to the point that they have caused a reversal of the previous southwesterly flow over the Indonesian archipelago. The flow is now an onshore southeasterly flow. Additionally the SE trades have begun to move the ITCZ north from  $5^{\circ}\text{S}$  to  $10^{\circ}\text{S}$ .

May shows a continuation of the pattern of the previous month (Figure 2.5a). The NE trades continue to weaken. They are more easterly in the central Pacific and veer along the Philippine coast to become indistinguishable from the SE trades. The SE trades have not yet become as strong as the NE trades in the central Pacific but they have changed the position of the ITCZ two-three degrees in latitude to a latitude band between  $2^{\circ}\text{S}$ - $7^{\circ}\text{S}$ .

In June (Figure 2.5b), the continuing strengthening of the SE trades in the western Pacific Ocean has pushed the ITCZ to the north of the equator. Cross-equatorial flow from south to north is now evident throughout the entire central and western tropical Pacific Ocean expanse. The strength of the wind stress field has changed only slightly from the previous month, the major change being this more pronounced cross-equatorial flow.



By July (Figure 2.6a), the influence of the summer heat low over Asia has resulted in a reversal of the wind flow along the Philippine coast from that of the January wind regime. The winds in the western tropical Pacific Ocean now have a southerly component as the SE trades continue to strengthen to a value of  $1.5 \text{ dyn cm}^{-2}$ . Northeast of Australia the influence of the southeasterlies has pushed the ITCZ to  $5^{\circ}\text{N}$ . The NE trades in the central Pacific have continued to weaken and are approximately  $1.0\text{-}1.2 \text{ dyn cm}^{-2}$ .

The pattern in August (Figure 2.6b) is little changed from the previous month. The ITCZ now spans latitudes  $7^{\circ}\text{-}9^{\circ}\text{N}$  in both the central and western Pacific Ocean basin.

The September wind stress pattern (Figure 2.7a) continues the summer pattern described in August. There is however a noticeable weakening ( $.2\text{-}.4 \text{ dyn cm}^{-2}$ ) of the SE trades in the western Pacific. The NE trades have also weakened (to values slightly above  $1.0 \text{ dyn cm}^{-2}$ ) and the ITCZ is now at  $10^{\circ}\text{N}$ , its furthest northward extension for this region of the Pacific.

As the SE monsoon dies out in October over east Asia, the NE trades begin to establish themselves again. This is evident over the western Pacific (Figure 2.7b) as the winds begin to reverse again along the Philippine coast. There is still, however, cross-equatorial flow from the SE trades. The ITCZ is nearer the equator in the western Pacific but maintains near  $10^{\circ}\text{N}$  in the central Pacific.

In November (Figure 2.8a), the NE trades show a pronounced increase in strength ( $0.5 \text{ dyn cm}^{-2}$ ) over the Philippine Sea. The SE trades have begun to retreat and there is now a broad area of very light winds from  $7^{\circ}\text{S}$  to  $7^{\circ}\text{N}$ . In the central Pacific, the

increase in the NE trades is also pronounced as the Asiatic cold high begins to build. There are two areas of convergent winds in the central Pacific, one along  $7^{\circ}\text{N}$  and a second but weaker one along  $10^{\circ}\text{S}$ .

In December (Figure 2.8b), the NE trades have again become dominant throughout the western and central equatorial Pacific Ocean. The NE winds turn along the northern New Guinea coast to become northwesterly. The pattern of two areas of trade wind convergence in the central Pacific makes the identification of the ITCZ difficult, there being convergence of SE and NE trades along both  $5^{\circ}\text{N}$  and  $12^{\circ}\text{S}$ .

Figures 2.9-2.14 illustrate the wind stress pattern for the eastern Pacific. The annual cycle is similar to the rest of the Pacific but the pattern is simpler and more regular. The NE trades are strongest in January (Figure 2.9a) and February (Figure 2.9b) when the SE trades are weakest as in the western Pacific. Six months later in July (Figure 2.12a) and August (Figure 2.12b) the reverse is true. Towards the American coastline the trade winds have a more north/south velocity component. This results in a more sharply defined and narrower convergence zone between the two trade wind systems. The ITCZ is located along latitude  $5^{\circ}\text{N}$  when the NE trades are strongest during the Northern Hemisphere winter (Figure 2.9) and is positioned at latitudes  $11-12^{\circ}\text{N}$  when the SE trade winds dominate in July and August (Figure 2.12).

To sum up, the high pressure center over the eastern Pacific off California coupled with the intense high pressure center over east Asia during the Northern Hemisphere winter cause the NE trades to be at their peak and dominate the SE trade wind flow in the western Pacific. During the Northern Hemisphere summer, the high center west of

California moves northwest, away from the equator and a high pressure center over the south Pacific moves north toward the equator, increasing the cross-equatorial flow of the SE trades and pushing the ITCZ north of  $10^{\circ}\text{N}$  in the eastern Pacific. The SE trades cross the entire length of the equator in July and August. In the western Pacific, the summer heat low over Asia and winter cold high over Australia act in tandem to cause strong southerly flow across the equator.

### III. RESULTS AND DISCUSSION

#### A. EDDY-RESOLVING NATURE OF THE GLOBAL MODEL

One of the significant features of the Semtner and Chervin general circulation global model is its high resolution ( $1/2^\circ$  horizontal grid spacing and 20 vertical levels). This enables the simulation to explicitly resolve mesoscale eddies in the tropics. The Rossby radius of deformation is the critical spatial scale numerical models need to resolve in order to accurately simulate oceanic boundary phenomenon such as fronts, eddies and boundary currents. The Rossby radius varies inversely with the Coriolis parameter  $f$ , which is given by

$$f = 1.47 \times 10^{-4} \sin \varphi \text{ s}^{-1},$$

where  $\varphi$  is latitude. For the mid-latitude oceans,  $\varphi = 45^\circ$ , the Coriolis parameter  $f = 1.0 \times 10^{-4} \text{ s}^{-1}$ . At  $10^\circ$  in the tropics the parameter  $f = 0.25 \times 10^{-4} \text{ s}^{-1}$ . This factor of four difference in the Coriolis parameter results in Rossby radius of deformation values typically 30-40 km for baroclinic waves in mid-latitudes and 120-160 km in the tropics (Gill, 1982). Thus tropical oceanic phenomenon should be accurately modeled by the 50 km horizontal resolution of the SC-GCM. The model also uses vertical and horizontal mixing values that are the smallest numerically allowed for the grid spacing. Additionally the use of biharmonic mixing in the horizontal allows spontaneous formation of eddies from instabilities without the undo suppression found from the use of Laplacian mixing in other model formulations (Semtner and Chervin, 1988).



The near-surface (37.5 meters) instantaneous current vector plots (Figures 3.1 and 3.2) of 15 May and 14 November in the model show a dominant train of anticyclonic eddies across the central and eastern Pacific between the equator and 5°N. In between these eddies and to the south can be seen smaller cyclonic eddies. The anticyclonic eddies appear to be generated from the horizontal shear zone between the eastward flowing North Equatorial Countercurrent (NECC) and the westward flowing South Equatorial Current (SEC). The modeled anticyclonic eddies have characteristic wavelengths of 800-1000 km, periods of 20-30 days and propagate westward with a phase speed of 40 km day<sup>-1</sup> (Tom Murphree, personal communication). They are most prominent in the summer and fall (Figure 3.2) when the SE trade winds are at their seasonal maximum and the modeled NECC and SEC reach their peak in response to this wind forcing.

The observational evidence to support the existence of these eddies is abundant. Legeckis (1977) first detected westward moving long waves in the eastern tropical Pacific from infrared images of a geostationary satellite in 1975. The satellite images displayed a wavelike temperature front between the SEC and NECC. A tongue of cooler water projected westward by the SEC results from the advection of upwelled water along the South American coast as well as upwelling along the equator from the divergence of Ekman transport. The NECC advects warmer water from the western Pacific. The satellite analysis of these long waves by Legeckis (1977) revealed wavelengths of 800-1200 km, periods of 20-30 days and phase speeds of 40 km day<sup>-1</sup>, matching the SC-GCM output. The waves are schematically shown in Figure 3.3. A companion study

of the instantaneous thermal field in the SC-GCM also reveals a wavelike temperature front between the SEC and NECC in the SC-GCM (Tom Murphree, personal communication). Interestingly, Legeckis noted a complete absence of these long waves in the satellite imagery during the following year, 1976, and related it to anomalous warming (4-6°C) in the eastern Pacific and weaker SE trades resulting in a weakening of the SEC and NECC. Further analyses of satellite imagery from 1975-1981 by Legeckis *et al.* (1983) showed these long waves occurred predominantly during the Northern Hemisphere summer and fall. They also occurred every year during the study except 1976 which subsequent research revealed was an El Niño year.

Subsequent studies of these long waves with satellite-tracked drifter buoys (Hansen and Paul, 1984) and comparisons of satellite SST with ship and moored buoy data (Pullen, et al, 1987) have revealed much about the properties of these waves. Hansen and Paul (1984) used drifter buoys to demonstrate that each trough in the temperature front contains an anticyclonic eddy and a smaller cyclonic eddy south of the crest of the waves. As can be seen in Figure 3.2 of the SC-GCM results, the model accurately simulates both of these eddies.

One difference noted between the model output and observations is that the model exhibits the anticyclonic eddies as far west as 165°E. Evidence from observations (Wyrtki, 1978) indicate that the furthest westward extent yet observed in these waves is 159°W. Their possible existence further west warrants investigation by oceanographers.

Barotropic instability from the shear zone between the SEC and NECC is believed to play a major role in the formation of these eddies (Philander, 1978), but another

simulation (Cox, 1980) successfully produced these waves and analysis indicated that baroclinic instability to also be an important secondary process. Furthermore, a model study by Semtner and Holland (1980) produced 20-30 day waves without a NECC, indicating that the role of barotropic instability in their formation is not certain. Further studies of the results in the SC-GCM are required.

The anticyclonic mesoscale eddies are easily resolved by upwards of 15-20 grid points in the SC-GCM. The SC-GCM additionally resolves the smaller cyclonic eddy features of wavelengths 100-200 km. A poorer resolution model would not be able to resolve these smaller features.

Mesoscale eddies have a critical influence on the mean circulation. They transport momentum and heat toward parts of the mean circulation and away from other parts. We are just beginning to understand the geographic distribution, size and dynamics of these mesoscale eddies. In parts of the equatorial Pacific, mesoscale eddies are so prevalent and strong, as in Figure 3.2, as to nearly totally obscure the mean flow. Nevertheless a qualitative description of the seasonal cycle in the tropical Pacific current system is evident in the vector plots. In the spring (Figure 3.1) the Equatorial Undercurrent (EUC) attains its maximum strength and can be seen as a dominant eastward flow along the equator at the 37.5 meter depth in the model. In this figure it appears that the EUC is gaining strength on its eastward journey. In actuality the EUC and its high velocity core shoals towards the east; *i.e.*, higher velocity isotachs are nearer the surface in the east than in the west. Six months later in November (Figure 3.2), the EUC has weakened and none of its isotachs is seen at the 37.5 meter level in the model

with the exception of eastward velocity on the equator between  $160^{\circ}$  and  $170^{\circ}$ E. In the late summer and fall, the southeasterly trades attain their maximum strength, and in response the SEC reaches maximum velocity and transport. The NECC similarly is at its peak magnitude and it is at this time that the modeled eddies are most prominent.

The extremely complicated nature of oceanic flow, particularly in highly variable regions such as the tropics is evident in these plots of instantaneous current vectors. Shipboard observations have difficulty in resolving the time and spatial scales of these types of flows. The immense expanse of water to be surveyed in the tropical Pacific and the high cost of ship time make numerical modeling of this region an important adjunct to oceanographic surveys in understanding the tropical oceanic circulation.

Another method of showing the instabilities of tropical currents is with time series graphs of temperature. Figures 3.4-3.7 begin with the last 2.5 years of the initial model experiment which used annual mean wind forcing. At the 2.5 year point in these figures the monthly mean wind forcing run begins. Average temperature from  $20^{\circ}$ S to  $20^{\circ}$ N at 200 meters is plotted at various longitudes across the Pacific. The top portion of each figure is a 3-day running mean which clearly indicates the intrinsic variability of the mean equatorial currents. Eddy activity is evident in both the annual mean and seasonal mean forcing portions of the graph with the strongest activity in the central Pacific along  $140^{\circ}$ W (Figure 3.6). The beginning of the seasonal cycle run at 2.5 years is quite evident. The steady rise in temperature during the last 2.5 years of the annual run is from a lack of intermediate-depth convection at higher latitudes. This warming trend is checked with the introduction of forcing by monthly varying winds. The seasonal cycle



run quickly reaches a quasi-equilibrium state. In the lower row of plots, high frequency variability is filtered out. These plots are 180-day and 360-day running mean temperature values. The 180-day averages clearly show a semi-annual signature in all the time series plots with minimum temperatures during the Northern Hemisphere summer and maximum in the winter. The summer temperatures are minimum as the upwelling along the equator as well as between the NEC and NECC are at their annual maximum.

## **B. MEAN ANNUAL STRUCTURE IN THE CENTRAL PACIFIC**

The seasonal cycle in the model of the tropical Pacific is analyzed in this study from archived monthly averaged tapes of standard oceanographic field variables of zonal velocity ( $u$ ), temperature ( $T$ ) and salinity ( $S$ ). The analysis of horizontal and vertical sections of these variables is simplified by using these tapes. Although the model appears to resolve quite realistically the complex structure of the tropical Pacific in the instantaneous plots as demonstrated in the previous section, a validation of the SC-GCM's ability to simulate the seasonal cycle in the equatorial Pacific by comparison with observations requires an analysis of averaged tapes. Because of the large annual and interannual variability of the wind field in the Pacific, a comparison of instantaneous fields from a climatologically forced model with observations would be misleading. The approach of this study is to use monthly averaged tapes and make comparisons with long-term observational studies. The forcing over the tropical Pacific while these observations were taken, while obviously never climatological, was at least typical and not anomalous,



*e.g.*, a non El Niño year. The complex eddy structure that is resolved by the model becomes averaged out from monthly mean tapes and the mean current flow can more readily be evaluated. Further averaging of the twelve monthly tapes for a given year produced an annual mean tape. Although the eddies are "filtered out" from the monthly and annual mean fields, their critical role and large influence in driving the mean circulation has been completed.

This section analyzes the annual mean tape for year four of the model run. As was seen in the time series of temperature (Figures 3.4-3.7), the model reaches a quasi-equilibrium state quickly after the introduction of seasonal forcing. (Year four of the seasonal run is year 6.5-7.5 in these figures.) Because of the lack of interannual variability in the forcing of the model, one model year looks very similar to any other year. The choice of year four in the model for analysis was arbitrary.

An analysis of the annual mean field in the model will provide the backdrop against which to understand the seasonal cycle of the Pacific equatorial current system and allow direct comparison of the output to results published in the observational literature. The mean annual near-surface (37.5 meters) tropical Pacific currents in the model are shown in Figure 3.8. Nearly all of the eddies and "wavy" structure previously seen in the instantaneous plots are no longer present. The currents in the mean are zonal. From 150°W to 100°W, the well-known pattern of alternating eastward and westward currents in the equatorial regions can be plainly seen. The eastward flowing EUC at the equator splits the flow of the SEC into a strong jet-like branch between the equator and 5°N and a weaker southern branch from 2°S to 6°S.

The mean annual meridional sections of zonal velocity, temperature and salinity in the model at 155°W longitude are compared to the mean annual sections from the Hawaii-to-Tahiti Shuttle Experiment conducted between 1979-1980 in the central Pacific. The sections from this experiment were analyzed by Wyrski and Kilonsky (1984). The model section and the observations show many striking similarities. Figures 3.9-3.11 show a side by side comparison between the model and the observations for zonal velocity, temperature and salinity.

Figure 3.9 and Table 3.1 (page 24) will be used to summarize the current comparisons between the model and the Hawaii-to-Tahiti Shuttle Experiment. The currents in both the observed and the modeled sections (Figure 3.9) are very similar both qualitatively and quantitatively. Both sections show a North Equatorial Current (NEC) with nearly the same latitudinal extent and with their 5 cm s<sup>-1</sup> isotach extending in depth near 300 meters. As in the observations, there appears a tendency for the NEC in the model to be split into two sections, a moderate flow of more than 20 cm s<sup>-1</sup> between 10°N and 15°N and a weaker flow of 5-10 cm s<sup>-1</sup> between 16 and 20°N in the model compared to between 16 and 18°N in the observations. The transports of the westward NEC is calculated at 25.2 Sv in the model and 23.3 Sv for the Shuttle experiment.

The North Equatorial Countercurrent (NECC) in both the model and in the observations extends from 4°N to 9°N. This eastward current has a higher velocity core in the observations than in the model (>40 cm s<sup>-1</sup> versus 27.7 cm s<sup>-1</sup>). The 5 cm s<sup>-1</sup> isotach extends past the 400 meter depth in the observations, and in the model this isotach stops very near 400 meters. This eastward flowing current north of the equator

is actually composed of two separate flows; the surface NECC and the deeper North Subsurface Countercurrent (NSCC). Both the model and observations show that these two eastward currents are connected, in the observations they are also connected to the EUC. Wyrski and Kilonsky (1984) used a velocity minimum at 170 meters depth to separate these two flows for purposes of evaluating the mean zonal transport of the two currents. Such a division in the model output is not evident, but for purposes of comparison, the model level of 160 meters was chosen to separate the NECC and NSCC. The transport of the surface flowing NECC is 19.8 Sv in the observations and 13.3 Sv in the model. The difference can largely be attributed to the higher core speed of the NECC in the observations.

The North Subsurface Countercurrent in both the model and the observations extends from 4° to 6°N. It also shows a mean observed zonal transport of 8.9 Sv and a transport of 6.7 Sv in the model.

The Equatorial Undercurrent for model and observations straddles the equator from 2°S to 2°N. The major difference is the larger vertical extent of this thin ribbon of eastward flow in the model. The model shows the currents extending to over 400 meters, whereas the observations show a reversal of the flow below 280 meters in the form of a westward flowing Equatorial Intermediate Current (EIC). The model also shows an EIC below the Undercurrent but it appears highly variable in time and space. The core velocity of the EUC is over 90 cm s<sup>-1</sup> at a depth of 130 meters in the observations and 111 cm s<sup>-1</sup> at a depth of 160 meters in the model. Profile current meter measurements of the EUC taken during the Shuttle Experiment gave a mean

transport for the EUC of 32.3 Sv and a maximum speed of  $102 \text{ cm s}^{-1}$ . In contrast, the model EUC, because of its much larger vertical extent, had a transport of 47 Sv. Other researchers (*e.g.*, Tchernia, 1980) give a mean transport for the EUC of 40 Sv, a value between the model results and the observations. Wyrтки and Kilonsky (1984) state that the EUC was unusually weak during the one-year period of their analysis.

The South Equatorial Current is divided into 3 separate sections in the analysis by Wyrтки and Kilonsky (1984). We will follow a similar strategy in the model for purposes of comparison.

Section 1 is the surface westward flow of the SEC from  $4^{\circ}\text{N}$  to the equator. This branch is much more restricted in the observations than in the model because of "sandwiching" by the connecting eastward flows of the NECC and the EUC. The maximum velocity in the Shuttle Experiment for the NECC is nearly  $90 \text{ cm s}^{-1}$  but only  $57.5 \text{ cm s}^{-1}$  in the model. The model, however, shows a much deeper vertical extent to this branch of the SEC because of the separation between the NECC and the EUC. The  $5 \text{ cm s}^{-1}$  isotach in the model extends beyond the 435 meter depth of the figure. The model transport for this section of the SEC is 19 Sv compared to 15.1 Sv for the observations.

Section 2 of the SEC in the model and the Hawaii-to-Tahiti Shuttle Experiment extends from the equator to  $9^{\circ}\text{S}$ . The  $5 \text{ cm s}^{-1}$  isotach for both is similar in depth of approximately 300 meters. The maximum velocity is  $42.6 \text{ cm s}^{-1}$  in the model and just over  $40 \text{ cm s}^{-1}$  in the observations. Transport for this branch is 26.5 Sv for the Shuttle experiment versus 31.5 Sv for the model. In both the model and the observations, this



section of the SEC has by far the highest transport relative to the other two westward sections.

Section 3 of the SEC is the westward flow south of  $9^{\circ}\text{S}$ . Embedded within this flow is the eastward flowing South Equatorial Countercurrent. The transport of this section of the SEC is 13.4 Sv in the observations and 8.3 Sv in the model. The model shows additional westward flow in this branch from  $20^{\circ}\text{S}$  to  $17^{\circ}\text{S}$  of an additional 8.3 Sv.

The total transport of the South Equatorial Current from its 3 sections from  $17^{\circ}\text{S}$  to  $4^{\circ}\text{N}$  is 55.0 Sv for the Shuttle Experiment and 58.8 Sv for the same latitudinal extent in the model. The additional flow in the model south of  $17^{\circ}\text{S}$  brings the total flow for the model's SEC to 67.1 Sv. Thus the SEC has the greatest magnitude of annual mean volume transport of all the equatorial Pacific currents. This can be attributed to the stronger and more extensive (latitudinally) SE trades as compared to the NE trades.

The South Equatorial Countercurrent (SECC) exhibits two branches of flow, a weak branch from  $8^{\circ}$  to  $10^{\circ}\text{S}$  and an even weaker branch at  $12^{\circ}\text{S}$  in the observations and  $16^{\circ}\text{S}$  in the model. The magnitude of the velocities of the flow compare favorably. Transport of only 0.6 Sv was calculated during the Shuttle Experiment and 1.2 Sv for the model's SECC. Although the South Equatorial Countercurrent is slightly stronger in the model than in the observations, both exhibit the similar split into two eastward branches.

The South Subsurface Countercurrent (SSCC) is weak in the model. With speeds of less than  $5 \text{ cm s}^{-1}$  and flow from  $4$ - $9^{\circ}\text{S}$  at 250-430 meters, the eastward zonal

**Table 3.1 COMPARISON OF MODEL TO SHUTTLE  
EXPERIMENT**

MEAN ANNUAL CURRENTS				
	MAXIMUM ZONAL VELOCITIES (cm s <sup>-1</sup> )		ZONAL TRANSPORT (Sv)	
CURRENT	SHUTTLE EX.	MODEL	SHUTTLE EX.	MODEL
NEC	20	20.6	23.3	25.2
NECC	40	27.7	19.8	13.3
SEC (eq. to 4°N)	90	57.5	15.1	19.0
SEC (eq. to 9°S)	40	42.6	26.5	31.5
SEC (9° to 17°S)	5	9.0	13.4	8.3
SEC (Total)	90	57.5	55.0	58.8
EUC	102	111.0	32.3	47.4
NSCC	10	21.8	8.9	6.7
SSCC	5	5.0	4.3	2.6
SECC	5	9.0	.6	1.2

transport is 2.6 Sv. The observations show a much stronger flow with a transport of 4.3 Sv. However, both the model and the observations show agreement with Tsuchiya (1975) in the relative strength of the South to the North Subsurface Countercurrent, i.e., the SSCC is half as intense as the NSCC.

Wyrski and Kilonsky (1984) also noted an unnamed westward flow below the NECC between 6° and 7°N that had a mean transport of 2.5 Sv. The model resolves a remarkably similar flow in the same area with a westward zonal transport of 2.7 Sv.

A comparison of model and observed temperature structure (Figure 3.10) shows the trough-ridge system that is a well-observed feature of the equatorial Pacific. The modeled thermocline comes very close to the surface at  $10^{\circ}\text{N}$  due to the upwelling caused by the strong Ekman divergence between the eastward flowing NECC and the westward flowing NEC. The thermocline also shows the characteristic spreading of the isotherms at the equator. This is associated with the EUC. Upwelling takes place above the EUC velocity core and downwelling below the core. The thermocline in the model does not have as sharp a vertical gradient of temperature as in the observations, but both observations and model show the thermocline beginning to deepen and spread as vertical temperature gradients decrease towards the poles north of  $10^{\circ}\text{N}$  and south of  $3^{\circ}\text{S}$ . The pools of warm water ( $27\text{-}28^{\circ}\text{C}$ ) at  $10^{\circ}\text{N}$  and  $10^{\circ}\text{S}$  are associated with the advection of warm water from the western Pacific by the eastward flowing NECC and SECC.

Close examination of the observed temperature section shows that, as Wyrtki and Kilonsky (1984) stated, the isotherms below the lower boundary of the thermocline are bent downward close to the equator, an indicator of the horizontal temperature gradients associated with the North and South Subsurface Countercurrents at  $5^{\circ}\text{N}$  and  $5^{\circ}\text{S}$ . The model shows a similar bending of the  $10^{\circ}$  and  $11^{\circ}\text{C}$  isotherms but evidently not a strong enough horizontal gradient to generate a strong South Subsurface Countercurrent.

The salinity distribution (Figure 3.11) shows many similarities between observations and simulations. The salinity increases southward across the equator until a high salinity cell is reached in the subtropical South Pacific. The subsurface salinity maximum is 36.1 psu in the thermocline and is very nearly identical to the observations.

Both sections show a tongue of high salinity water in the southern tropics penetrating to the equator and into the EUC. There is another salinity maximum in the thermocline north of the equator. It penetrates southward to about  $15^{\circ}\text{N}$  in the model but  $11^{\circ}\text{N}$  in the observations. Both sections exhibit the salinity minimum in the northern tropics rising up from a depth of over 400 meters at  $20^{\circ}\text{N}$  to a depth of 100 meters at  $10^{\circ}\text{N}$ .

### C. SEASONAL CYCLE IN THE EQUATORIAL PACIFIC

The seasonal variation of the surface winds over the equatorial Pacific Ocean determine the location of the Intertropical Convergence Zone (ITCZ), the area of light winds between the converging trade wind systems of the Northern and Southern Hemisphere. When the equatorial trade winds are weak during the Northern Hemisphere spring, the ITCZ is near the equator. The surface currents are weak and the Equatorial Undercurrent (EUC) is at its peak. Figure 3.12 shows near-surface (37.5 meters) current vectors in the east central Pacific during the month of May. Most of the 30-day and shorter period waves have been averaged out. The EUC dominates the flow with its high velocity jet along the equator.

Figure 3.13 depicts average currents during the month of November. The ITCZ has shifted northward to near  $10^{\circ}\text{N}$  in the eastern Pacific. The southeast trades are strong and the surface currents respond by reaching maximum velocities. The SEC attains speeds in excess of  $90\text{ cm s}^{-1}$  and a latitudinal extent of  $5^{\circ}\text{S}$ - $5^{\circ}\text{N}$ . The NECC can be followed unbroken across the entire tropical Pacific, achieving velocities of over  $65\text{ cm s}^{-1}$ . The NEC continues to remain a relatively weak flow with only a minor



seasonal signature but does appear better organized than in the spring. Its velocities approach  $20\text{--}30\text{ cm s}^{-1}$ . The EUC does not surface during November and is significantly weaker than in the spring with a maximum velocity of  $118\text{ cm s}^{-1}$  at  $131^\circ\text{W}$ .

A meridional section along  $160^\circ\text{W}$  (Figure 3.14) shows zonal velocity from  $20^\circ\text{S}$  to  $20^\circ\text{N}$  for the months of May and November. The EUC decreases in velocity from  $121\text{ cm s}^{-1}$  to  $96.5\text{ cm s}^{-1}$ . The depth of its maximum velocity core changes from 117.5 meters to 160.0 meters as it weakens and submerges. In contrast the North Equatorial Countercurrent nearly doubles in velocity from  $25\text{ cm s}^{-1}$  to  $49\text{ cm s}^{-1}$ . Likewise, the South Equatorial Current increases from  $36.0\text{ cm s}^{-1}$  in the spring to  $62.1\text{ cm s}^{-1}$  in the fall. The North Equatorial Current does not appear to have a strong seasonal fluctuation, both the spring and the fall velocities are in the neighborhood of  $20\text{ cm s}^{-1}$ . The eastward flowing South Equatorial Countercurrent shows a similar pattern to its northern counterpart. It is a weak  $4\text{ cm s}^{-1}$  in the spring and increases significantly in velocity in the fall to over  $15\text{ cm s}^{-1}$ .

The temperature structure exhibits a strong seasonal signature in the area between the North Equatorial Countercurrent at  $9^\circ\text{N}$  and the branch of the South Equatorial Current north of the equator. In the spring the thermocline has a weak trough near  $3^\circ\text{N}$  and a slight ridge at  $10^\circ\text{N}$ . Latitudinal temperature gradients are relatively weak. The situation is reversed in the fall. The meridional temperature sections in Figure 3.15 show this remarkable seasonal change to the isotherm pattern. The well-observed pattern of isothermal spreading of the thermocline from the influence of the EUC is also resolved

well in the model. The isotherms in the fall are pushed upward considerably by the upwelling at 10°N, creating a strong horizontal temperature gradient across the front.

The seasonal variation in salinity structure of the model at 160°W is quite small (Figure 3.16). The front that exists in the fall between the NECC and the SEC generates a salinity front in addition to the temperature front previously mentioned. This can be seen in the vertical isohalines between 5°N and 10°N which separates the salty water along the equator from the slightly fresher water to the north.

Another view of the seasonal changes in current structure along the equator is shown in Figure 3.17. This represents zonal velocity in the model as an equatorial section to a depth of 310.0 meters. Several striking features stand out. The top figure of flow in May shows that the EUC reaches a maximum strength of  $148 \text{ cm s}^{-1}$  at 130°W at a depth of 117.5 meters. There is eastward flow at nearly all depths along the equator as far west as 140°E where the current is very deep (222.5 meters), but it appears that the EUC is a poorly organized flow until it approaches the international dateline. During the spring months the EUC surfaces and there is eastward flow along the surface from 175°W to near the South American continent. In November the modeled EUC shows a maximum velocity of  $118 \text{ cm s}^{-1}$ , again along 130°W longitude but at a deeper 160 meters depth. At this time of the year, the flow at the surface along the equator is westward under the influence of the SE trades. Another feature of the model's EUC is the pronounced upward slope toward the east of the velocity core. This is characteristic of the observations of the EUC as it straddles the upward sloping thermocline on its eastward journey across the Pacific.

Figure 3.18 is a time-longitude plot at the first vertical level of the model (12.5 meters) that shows zonal velocity along the equator as a function of time. The surfacing of the EUC is first seen in the spring commencing in the eastern Pacific.

The seasonal fluctuations in zonal volume transport in Sverdrups for the NECC, EUC and SEC at various longitudes are shown in Figure 3.19. The SEC and the NECC are in phase with each other and out of phase with the EUC as previously mentioned. Figure 3.20 shows the variability in the transport of the NEC. No coherent seasonal cycle is evident with this westward flow.

#### **D. WESTERN EQUATORIAL PACIFIC**

The currents in the western Pacific are of an extremely complex nature due to monsoon cycle forcing which causes a reversal of the wind stress, and due to the complex topography represented by the hundreds of islands of the Philippines and of the Indonesian Archipelago. Many of the equatorial Pacific currents terminate or originate in this region and the treatment of the islands in numerical models determines to a great extent the accuracy of the reproduced currents. Figure 3.21 represents the observed current structure during February and August in the western Pacific. The NEC bifurcates along the Philippine island of Mindanao with a portion of its flow heading northwest to form the beginnings of the Kurishio and the remainder of its transport deflecting to form the start of the NECC. The SEC joins the surfaced New Guinea Undercurrent on the north side of that island and is turned by the island of Halmahera

to join in forming the beginning of the NEC. The importance of Halmahera in the current structure is seen in the historical ship drift observations in Figure 3.22.

The SC-GCM in its global formulation was forced to make compromises with the global topography in order to make the global calculation tractable. Many of these topographic compromises were made in the western Pacific because of the large number of islands there. For example, the islands of Mindanao and Halmahera were shoaled. This results in model currents for the western Pacific seen in the vector plot of Figure 3.23. Since Mindanao is shoaled, the NEC flows to the coast of Borneo ( $5^{\circ}\text{N}$ ,  $120^{\circ}\text{E}$ ) and is shunted toward the south to form an intense unstable current along the coast in the Makassar strait. The large anticyclonic eddy just north of the equator between  $120^{\circ}\text{E}$  and  $130^{\circ}\text{E}$  becomes a semi-permanent feature in the model calculation and represents the origin of the eastward flowing NECC. The fact that the central Pacific currents in the model examined earlier compared so well to observations indicates that the treatment of the islands in the west and the boundary they represent are quickly "forgotten" by the currents after having reached the central Pacific region.



#### IV. CONCLUSIONS AND RECOMMENDATIONS

The Semtner and Chervin global ocean model reproduces many of the known features of the seasonal cycle of the tropical Pacific Ocean. Current structure, velocity and seasonal variability show remarkably realistic features. However, many of the details of these plots have no corresponding observations with which to make direct comparisons. The observations that are available often cannot be meaningfully compared to model output because of the difference in wind forcing at the time observations were taken from the climatological wind forcing in the model.

Temperature and zonal velocity patterns fit the descriptions of these fields in the observational literature. One notable exception is that the observed mixed layer depths, particularly in the western Pacific, are deeper than in the model. The model tends to have a diffuse thermocline. Philander *et al.* (1987) noted very similar results from his model studies and believed that the poor mixing might be attributed to the lack of high-frequency wind fluctuations in the climatological wind forcing fields.

A detailed analysis of the mass and heat budgets from the SC-GCM needs to be made to ascertain the model's performance in these areas. Similar analyses and comparisons with the results of the model in other tropical regions and with other regional models should also be made. Analysis of the deep equatorial flow would be of interest to determine if the off-equatorial and deep equatorial jets that have been observed



are resolved. These deep equatorial jets have also appeared in model studies by McCreary (1987).

The complexity of oceanic flow in the western Pacific requires a more sophisticated treatment of islands in the model in order for this area to show more realism. Killworth *et al.* (1991) have developed a free-surface effect that should make calculations involving islands tractable.

Improvement in the horizontal and vertical resolution of the model, while desirable, would not likely improve the model results as much as improving the climatological forcing of wind and heat. A test of the model using observed wind forcing, particularly incorporating interannual variability, would be of great interest.

## APPENDIX (FIGURES)

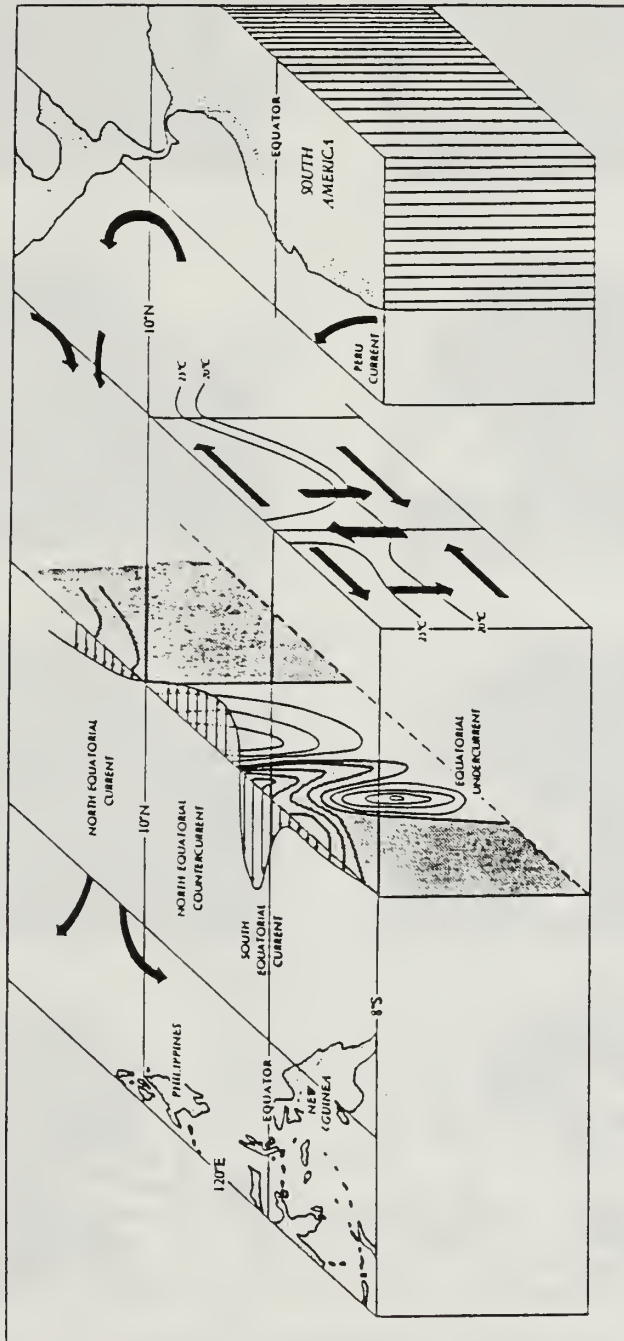


**Figure 1.1** A schematic diagram of upper tropical Pacific Ocean circulation (from Philander *et al.*, 1987)

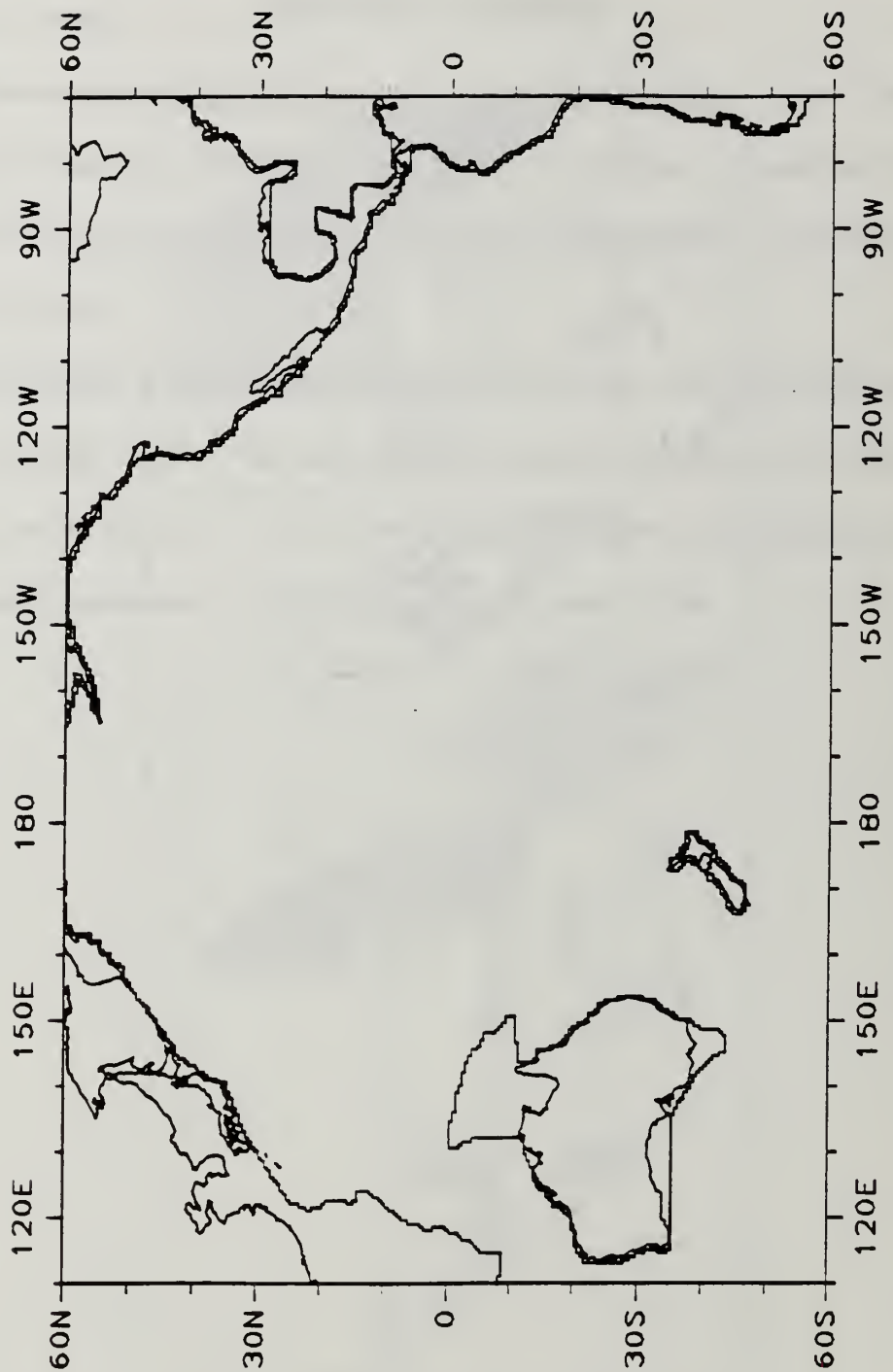
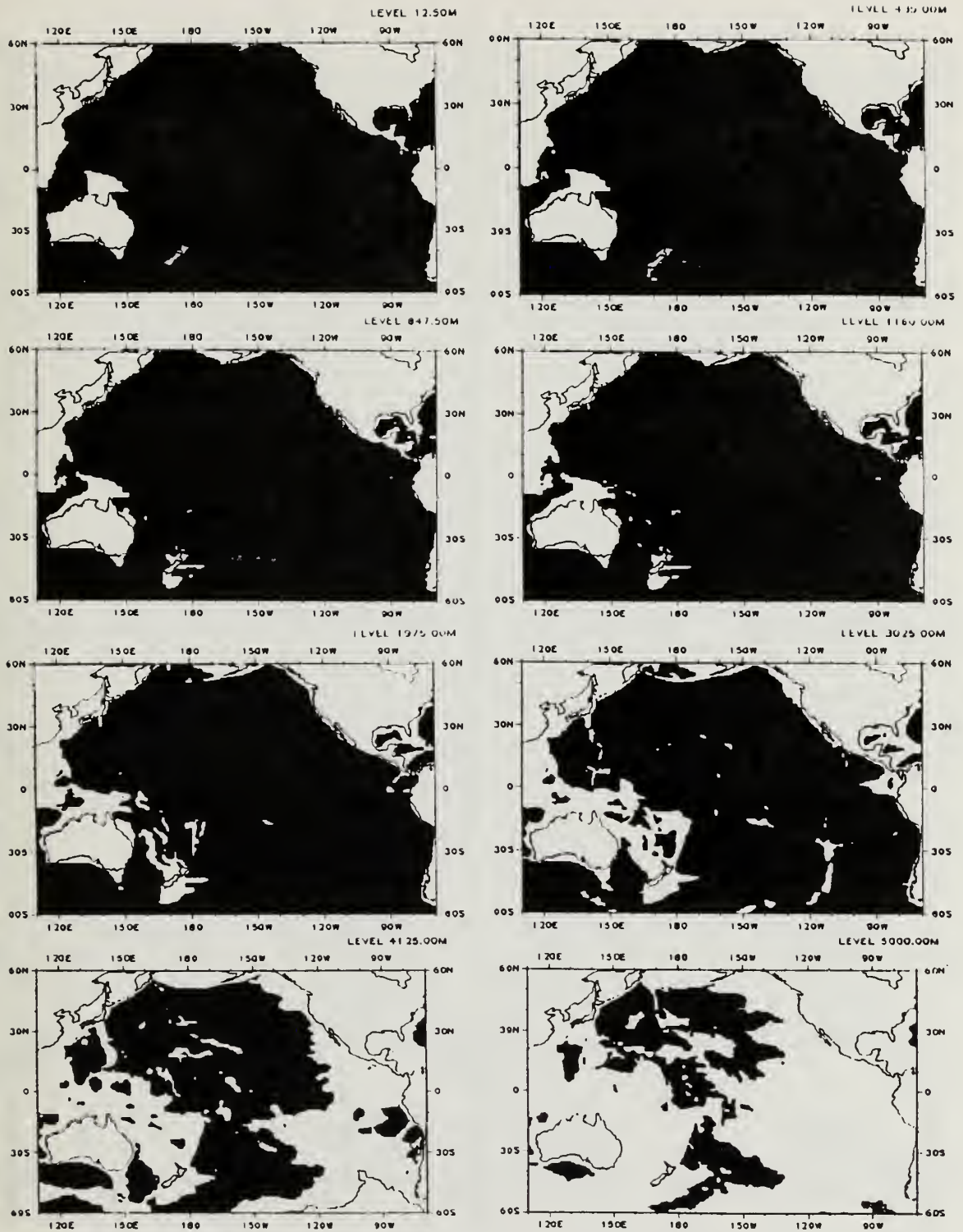


Figure 2.1 The global ocean model domain for the Pacific Ocean.



**Figure 2.2** Global ocean model bathymetry for the Pacific Ocean at various depths. (a) 12.5 m, (b) 435 m, (c) 847.5 m, (d) 1160 m, (e) 1975 m, (f) 3025 m, (g) 4125 m, (h) 5000 m.





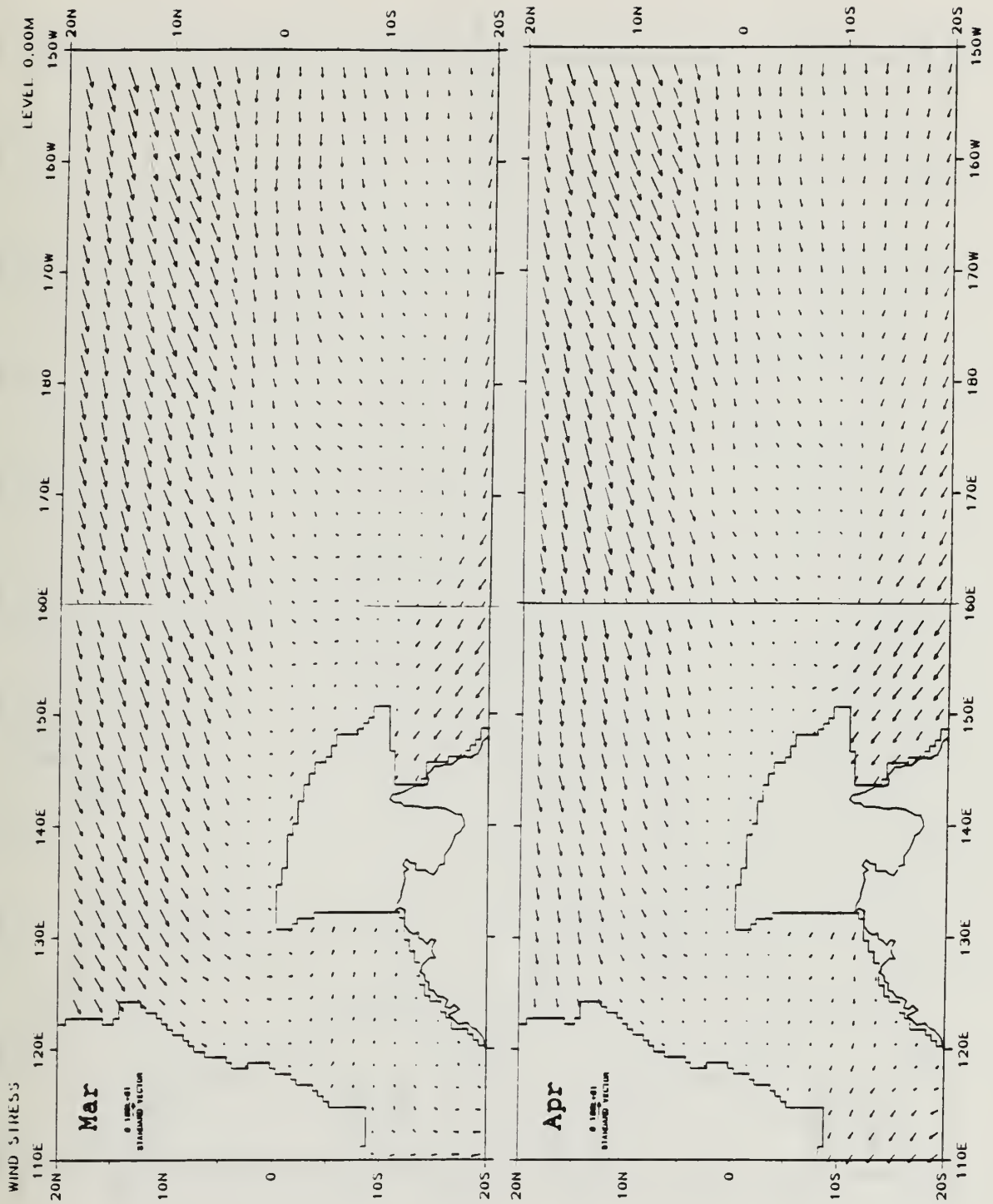


**Figure 2.4** Hellerman and Rosenstein (1983) mean wind stress in western and central Pacific for: (a) March and (b) April. Standard vector length =  $1 \text{ dyn cm}^{-2}$ .

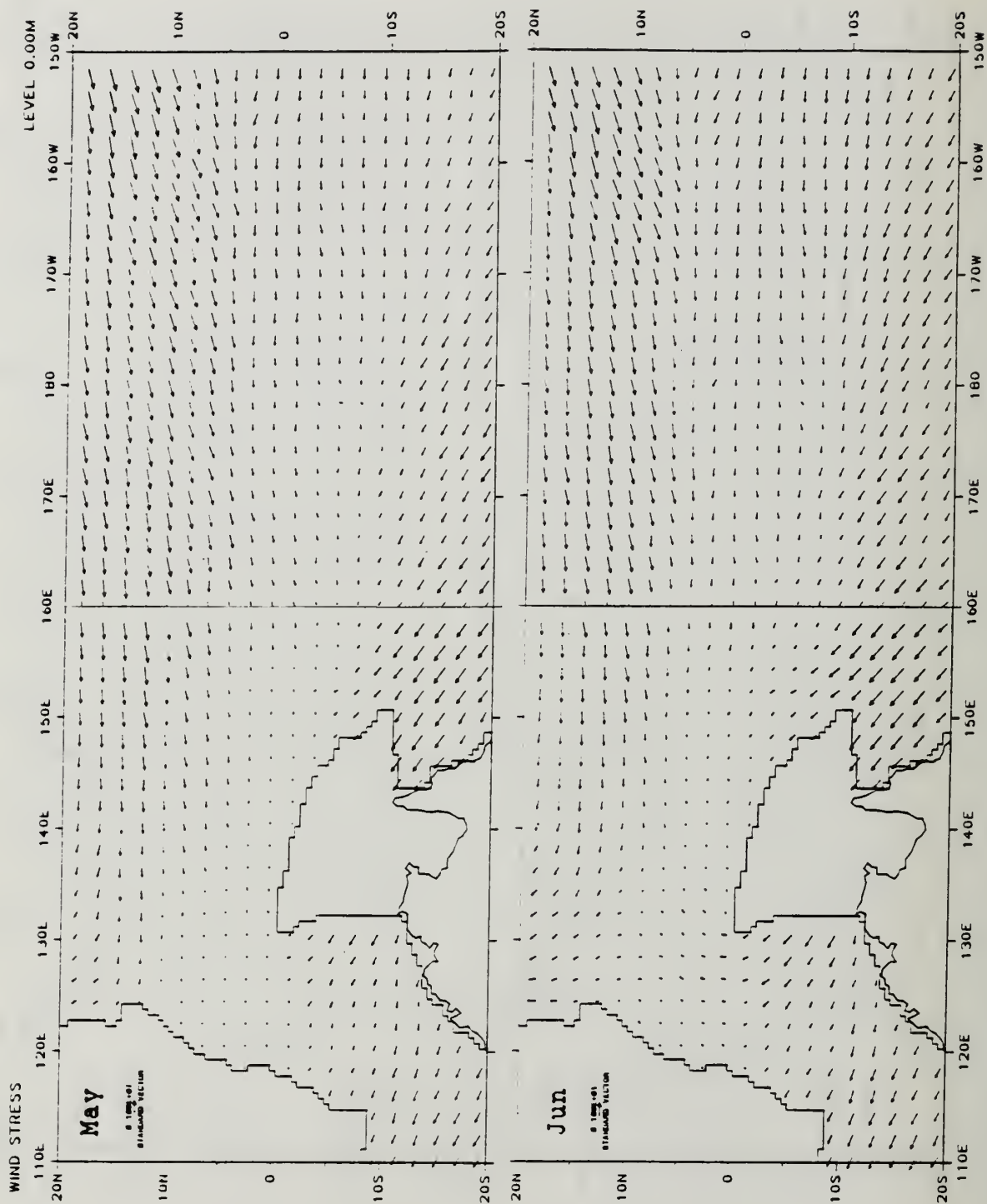


**Figure 2.5** Hellerman and Rosenstein (1983) mean wind stress in western and central Pacific for: (a) May and (b) June. Standard vector length =  $1 \text{ dyn cm}^{-2}$ .

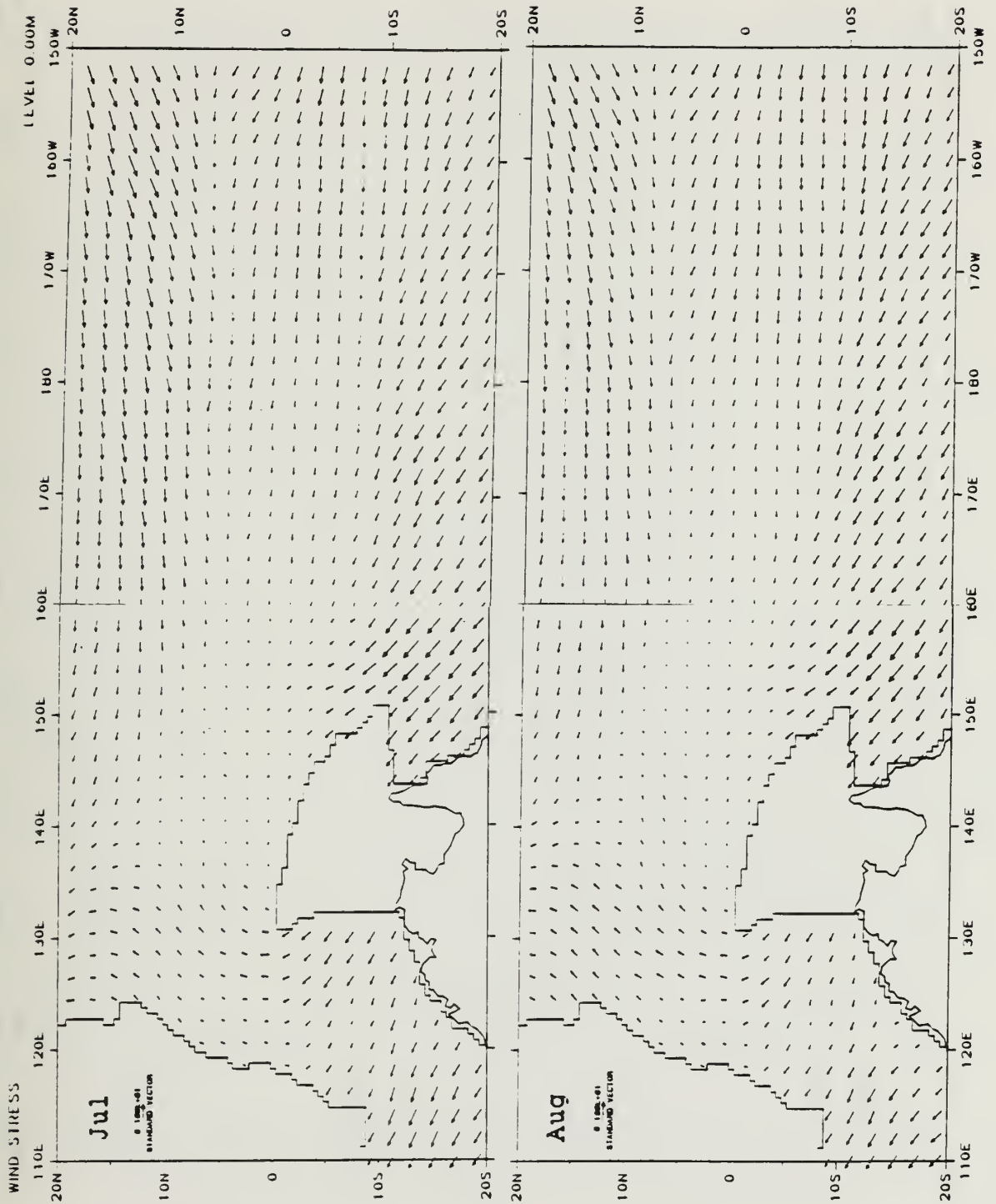


**Figure 2.6** Hellerman and Rosenstein (1983) mean wind stress in western and central Pacific for: (a) July and (b) August. Standard vector length =  $1 \text{ dyn cm}^{-2}$ .



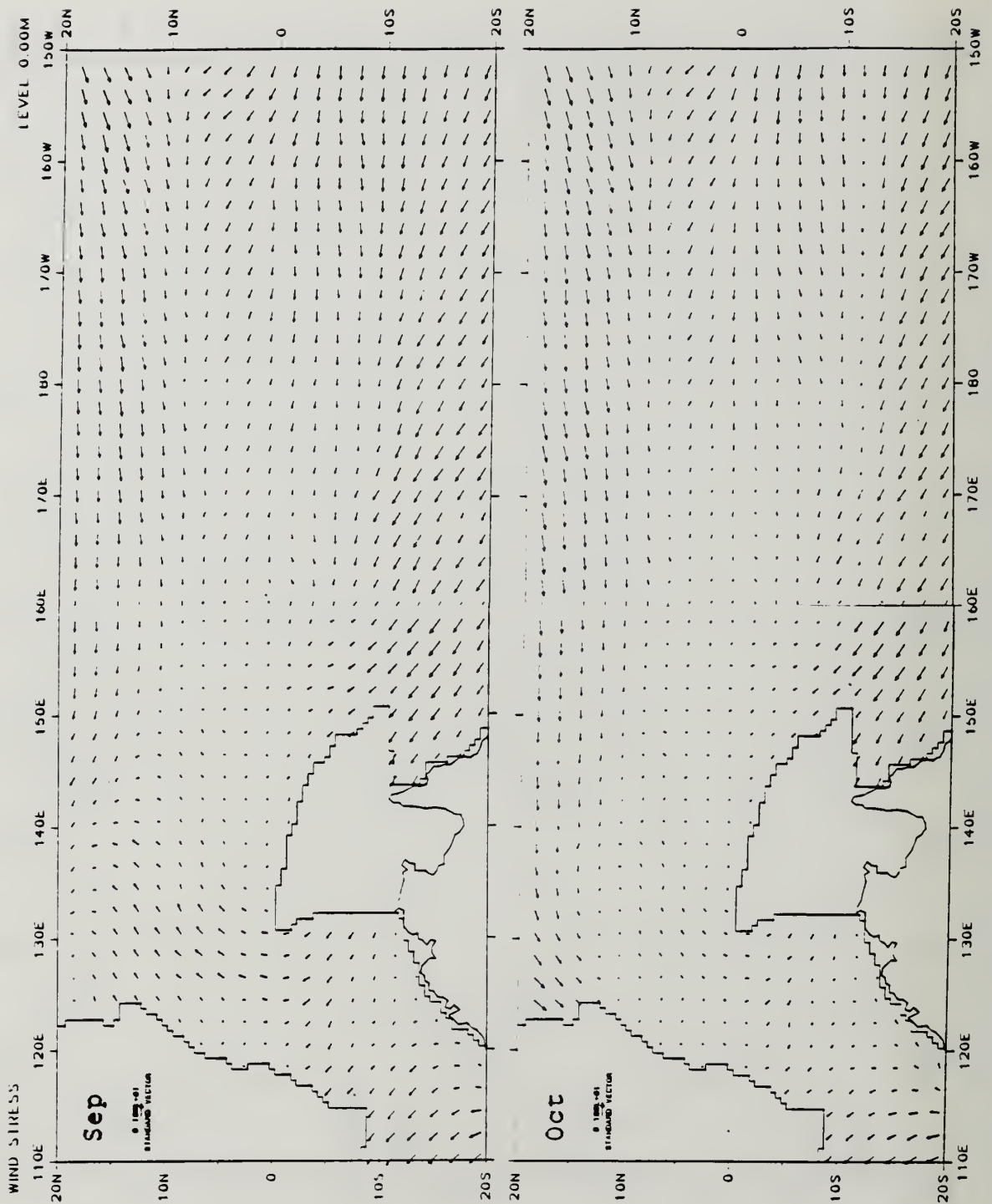


**Figure 2.7** Hellerman and Rosenstein (1983) mean wind stress in western and central Pacific for: (a) September and (b) October. Standard vector length = 1 dyn cm<sup>-2</sup>.

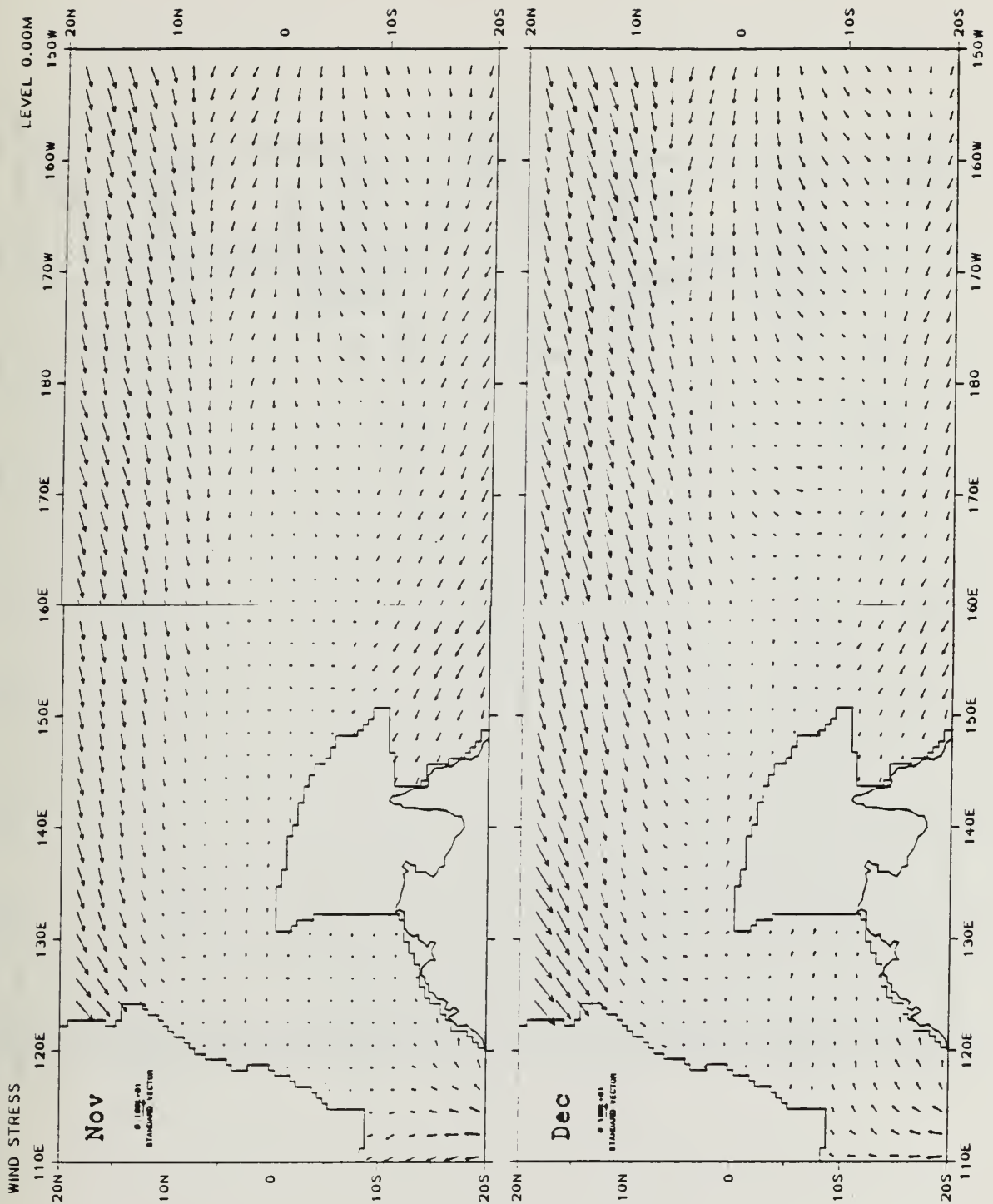


**Figure 2.8** Hellerman and Rosenstein (1983) mean wind stress in western and central Pacific for: (a) November and (b) December. Standard vector length =  $1 \text{ dyne cm}^{-2}$ .

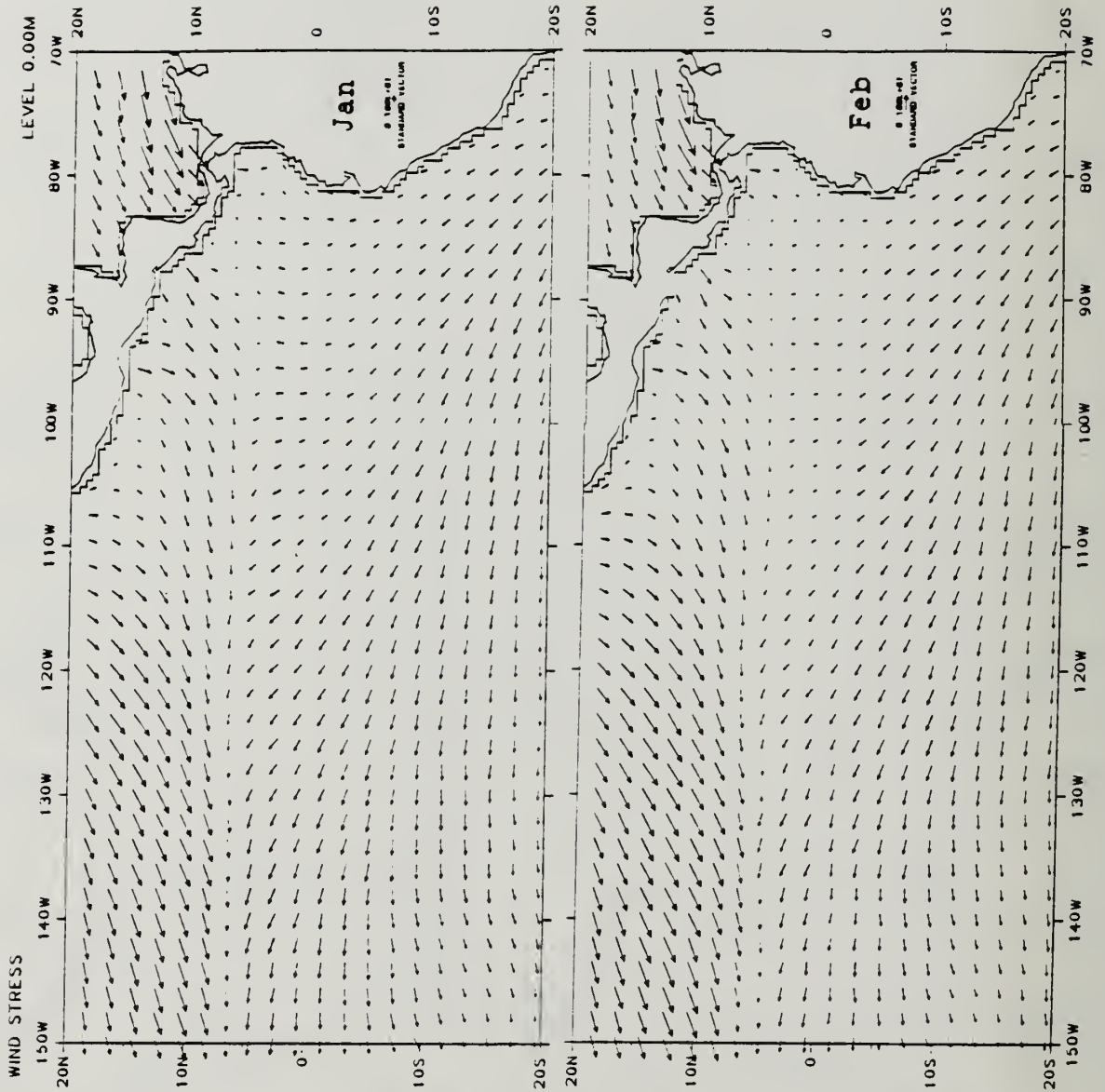


**Figure 2.9** Hellerman and Rosenstein (1983) mean wind stress in eastern Pacific for: (a) January and (b) February. Standard vector length =  $1 \text{ dyn cm}^{-2}$ .

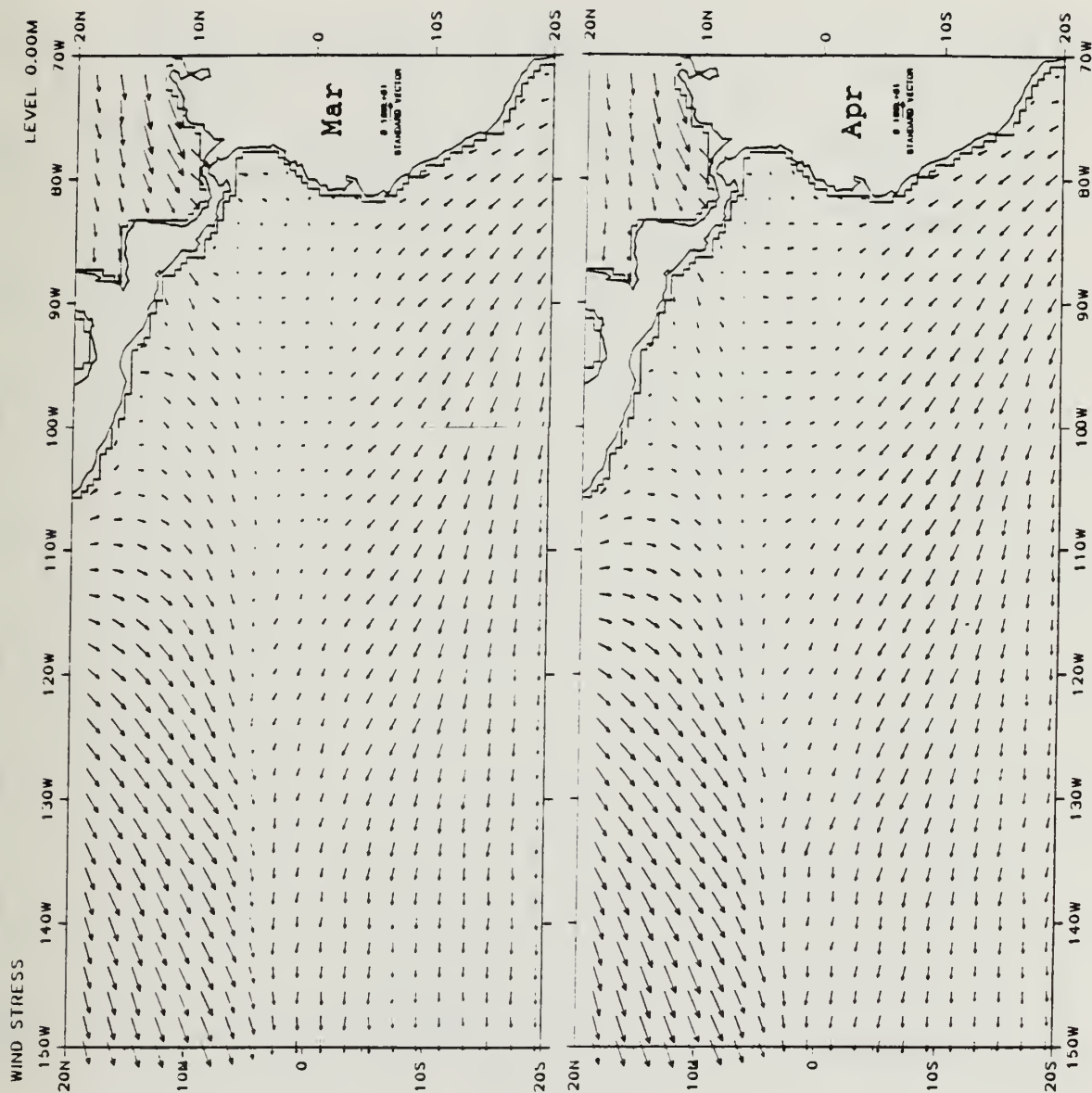


**Figure 2.10** Hellerman and Rosenstein (1983) mean wind stress in eastern Pacific for: (a) March and (b) April. Standard vector length =  $1 \text{ dyn cm}^{-2}$ .



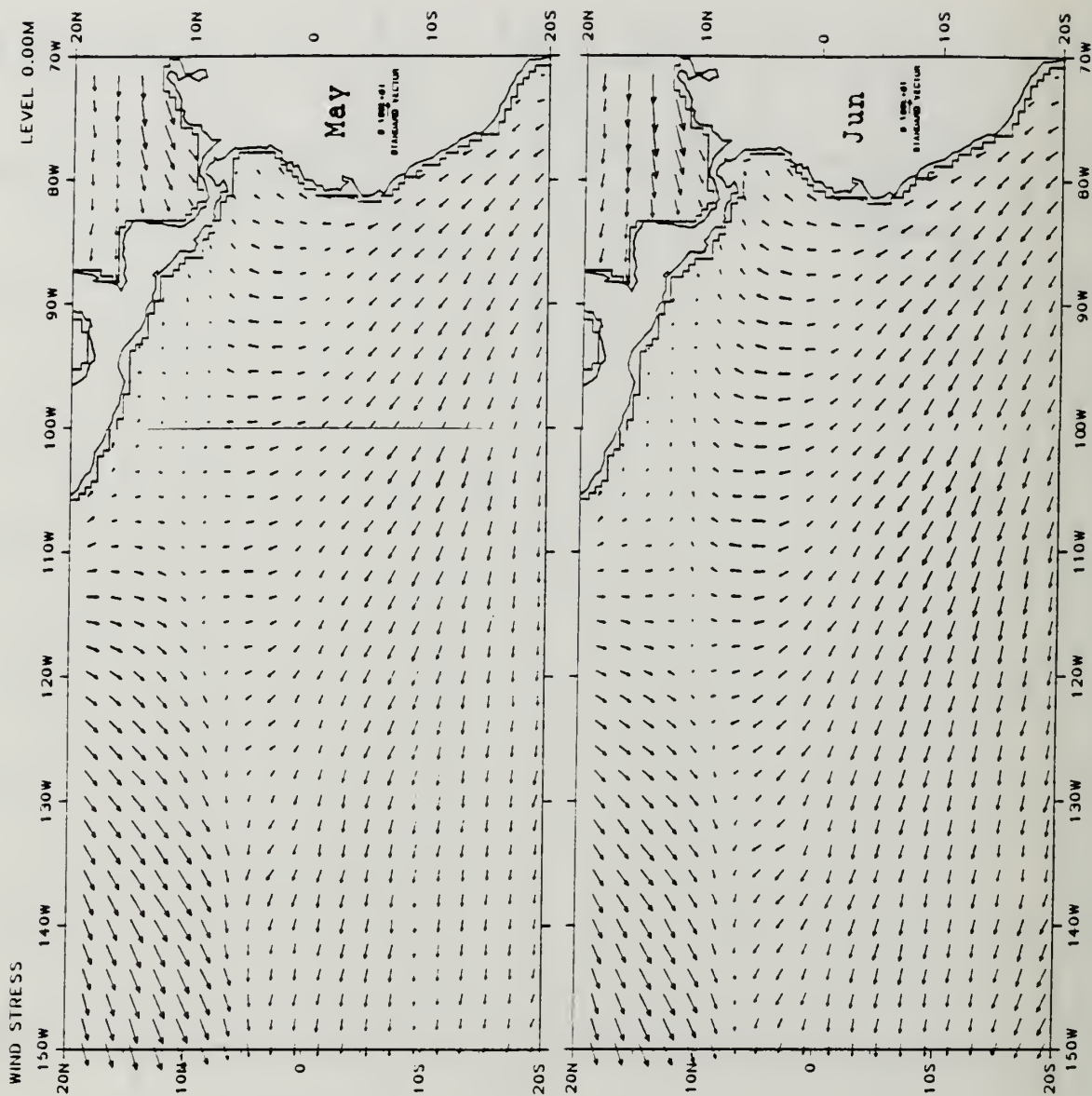


**Figure 2.11** Hellerman and Rosenstein (1983) mean wind stress in eastern Pacific for: (a) May and (b) June. Standard vector length =  $1 \text{ dyn cm}^{-2}$ .

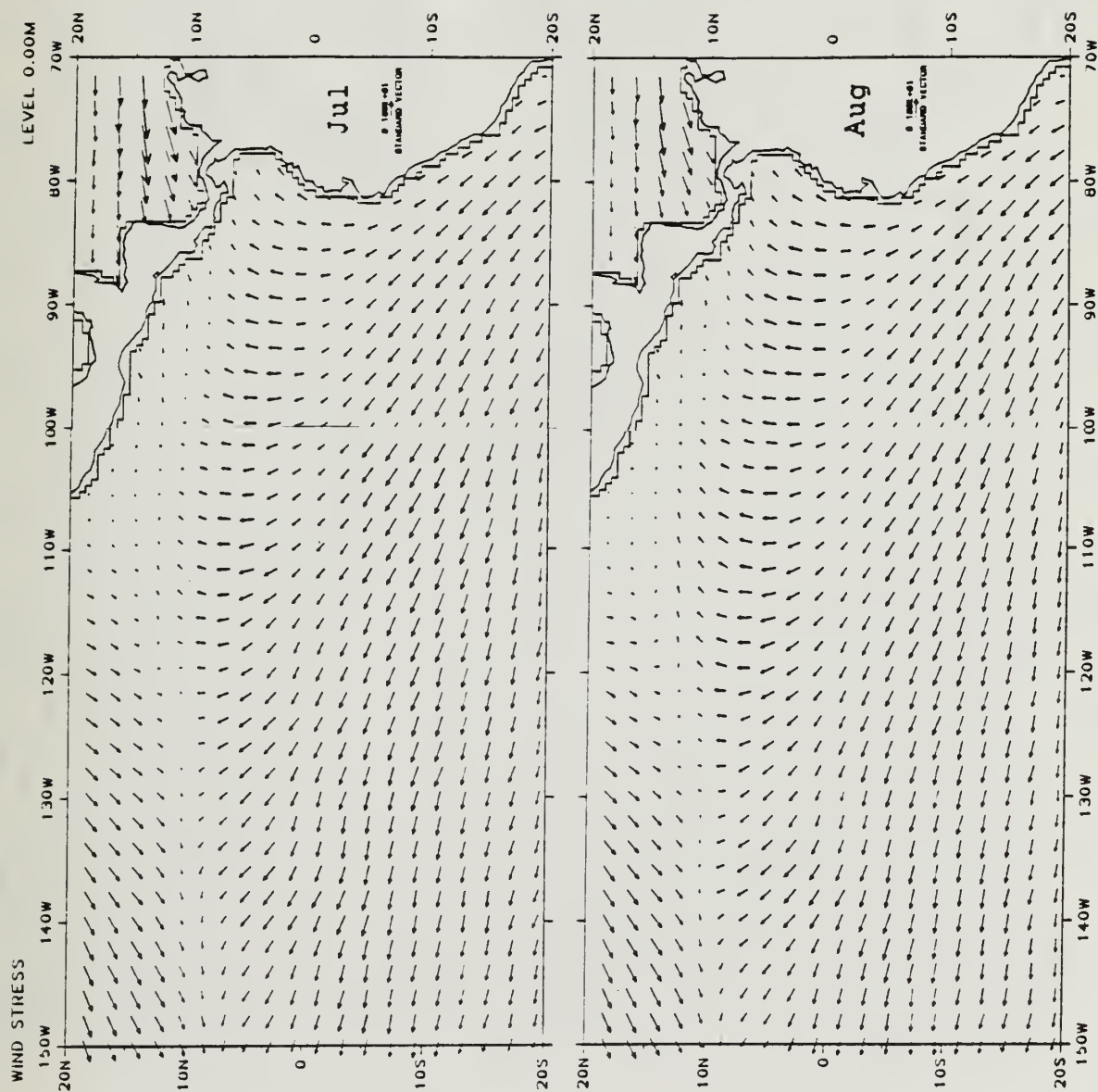


**Figure 2.12** Hellerman and Rosenstein (1983) mean wind stress in eastern Pacific for: (a) July and (b) August. Standard vector length =  $1 \text{ dyn cm}^{-2}$ .

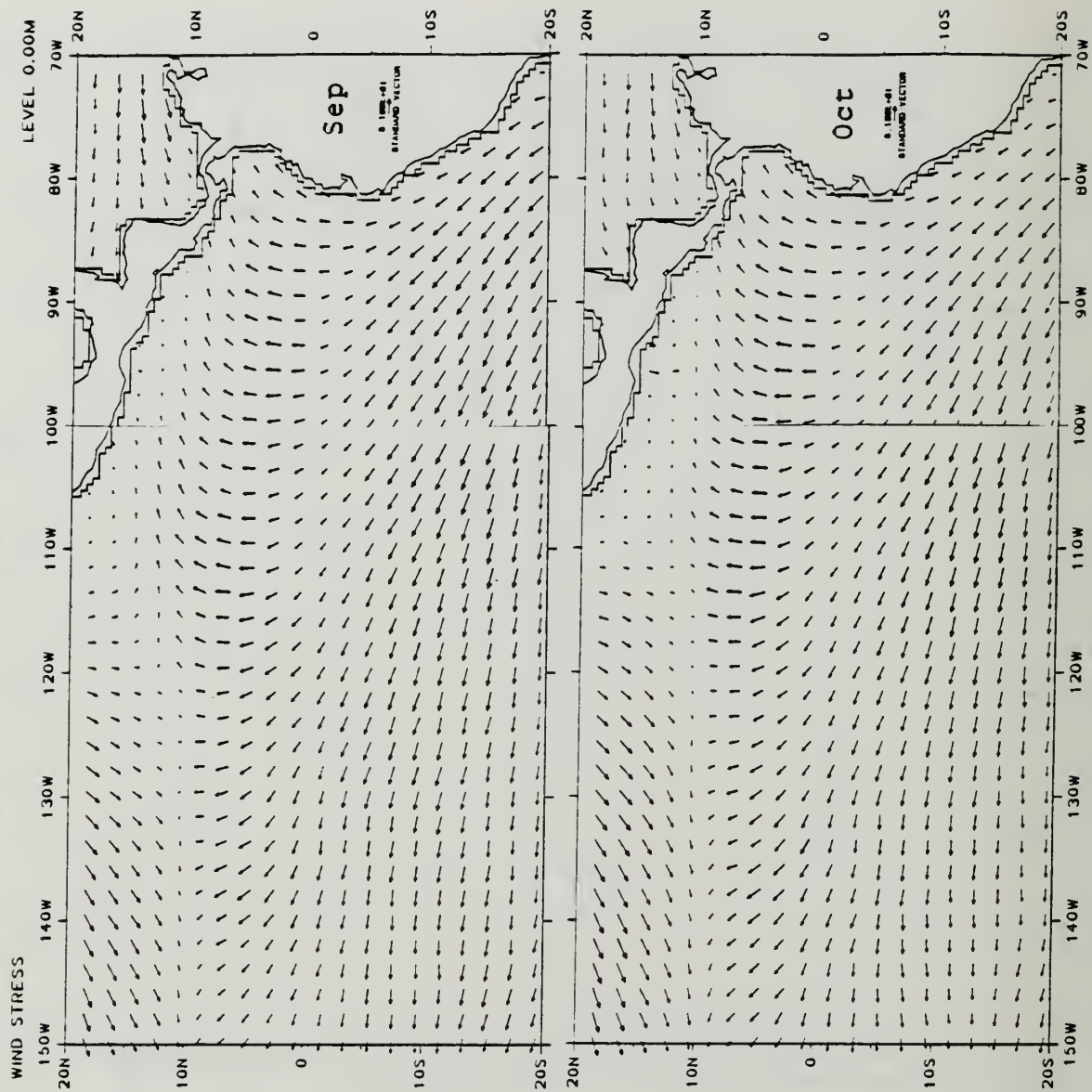


**Figure 2.13** Hellerman and Rosenstein (1983) mean wind stress in eastern Pacific for: (a) September and (b) October. Standard vector length =  $1 \text{ dyn cm}^{-2}$ .

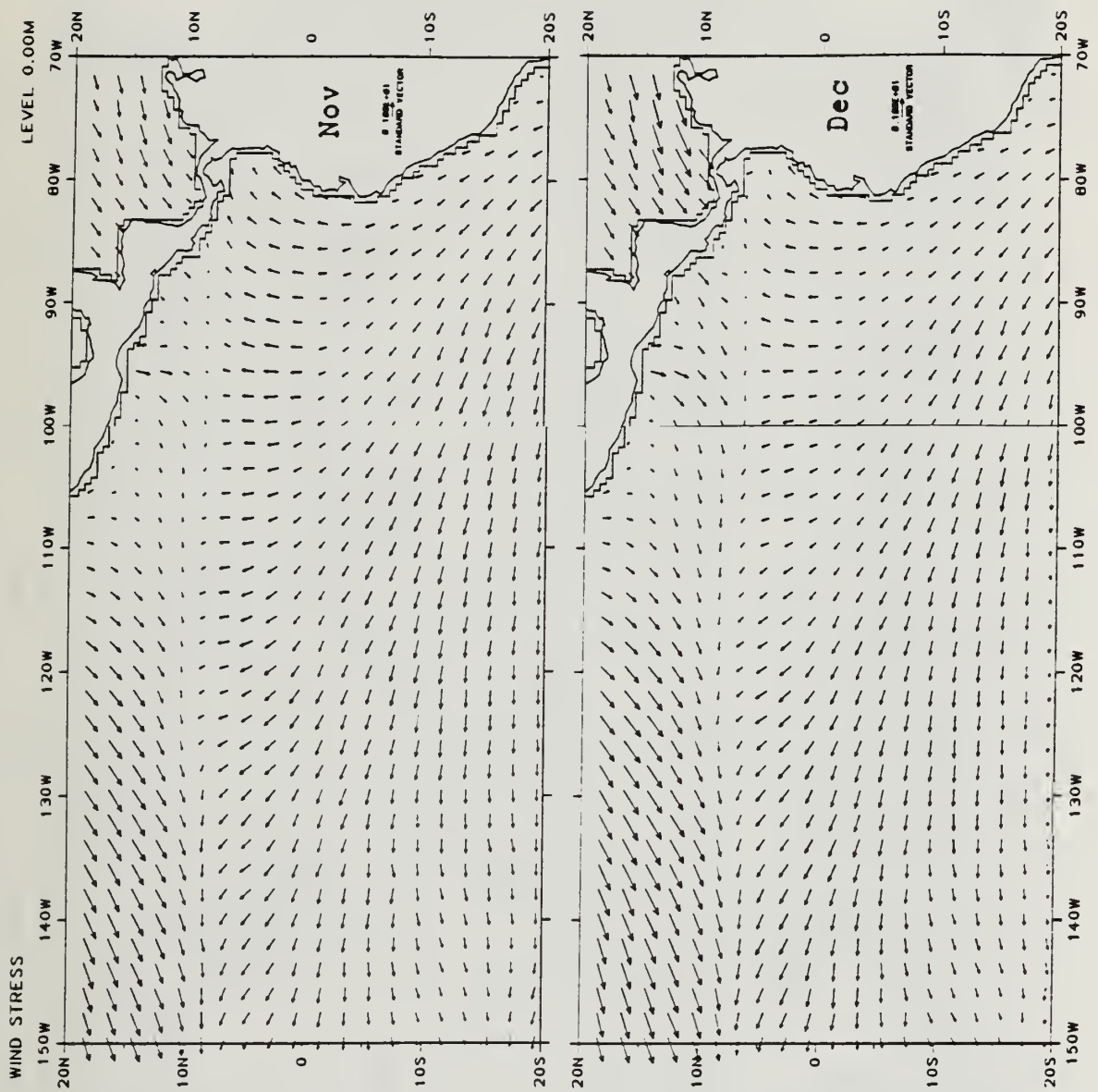


**Figure 2.14** Hellerman and Rosenstein (1983) mean wind stress in eastern Pacific for: (a) November and (b) December. Standard vector length =  $1 \text{ dyn cm}^{-2}$ .



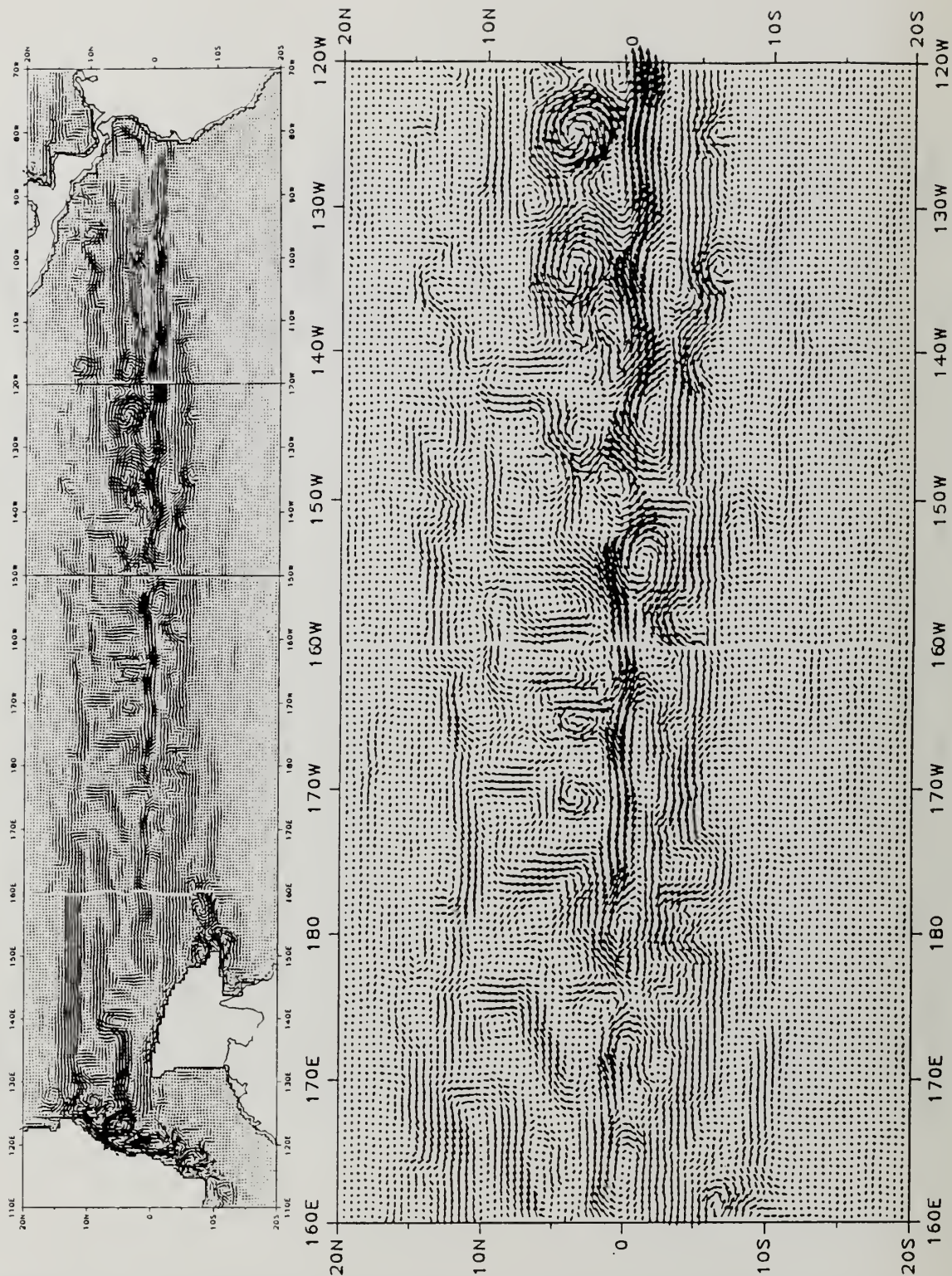


**Figure 3.1** Instantaneous current vectors at 37.5 meters for 15 May, year 4 of seasonal model run. a) Pacific basin b) Central eastern Pacific.



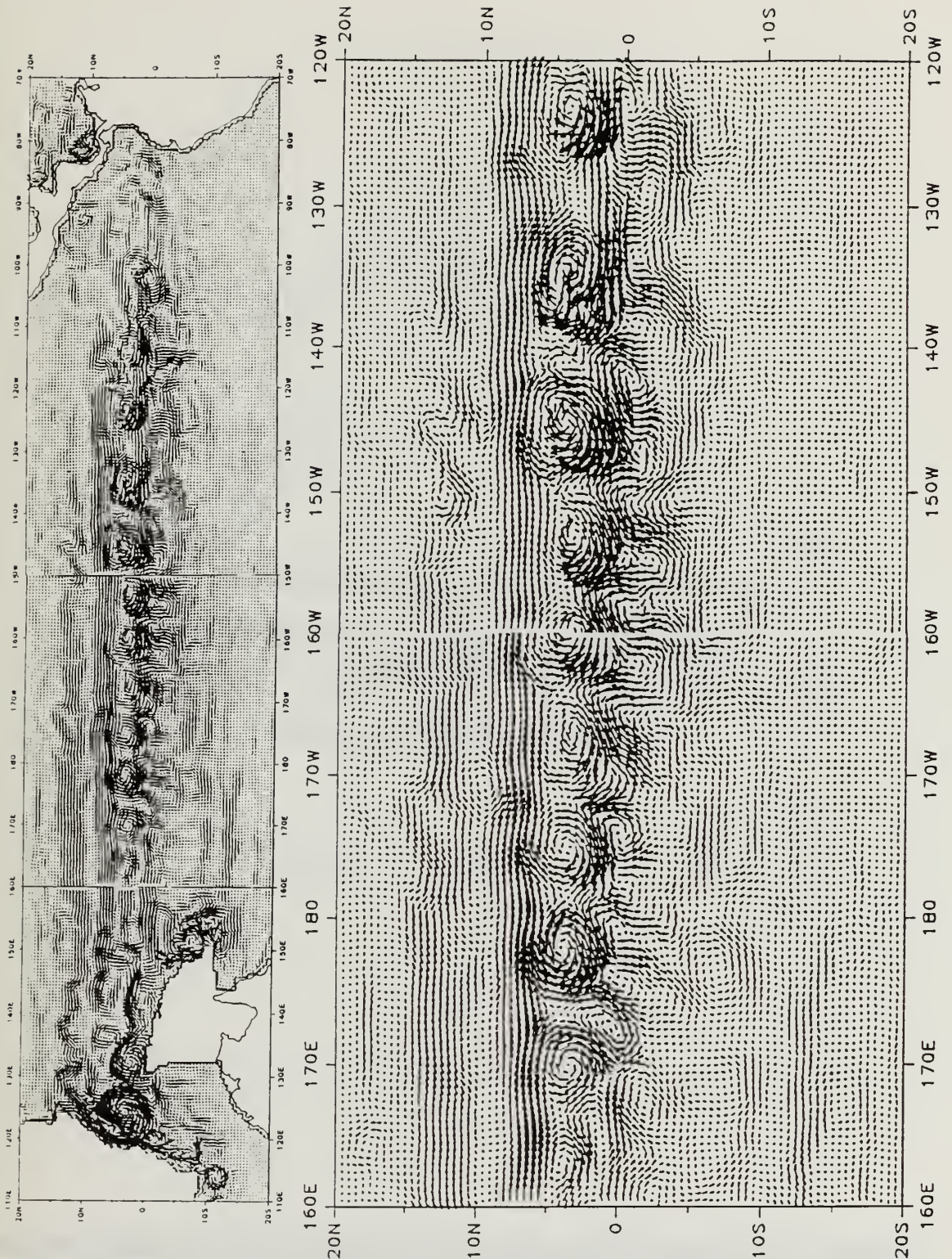


**Figure 3.2** Instantaneous current vectors at 37.5 meters for 14 November, year 4 of seasonal model run. a) Pacific basin b) Central eastern Pacific.

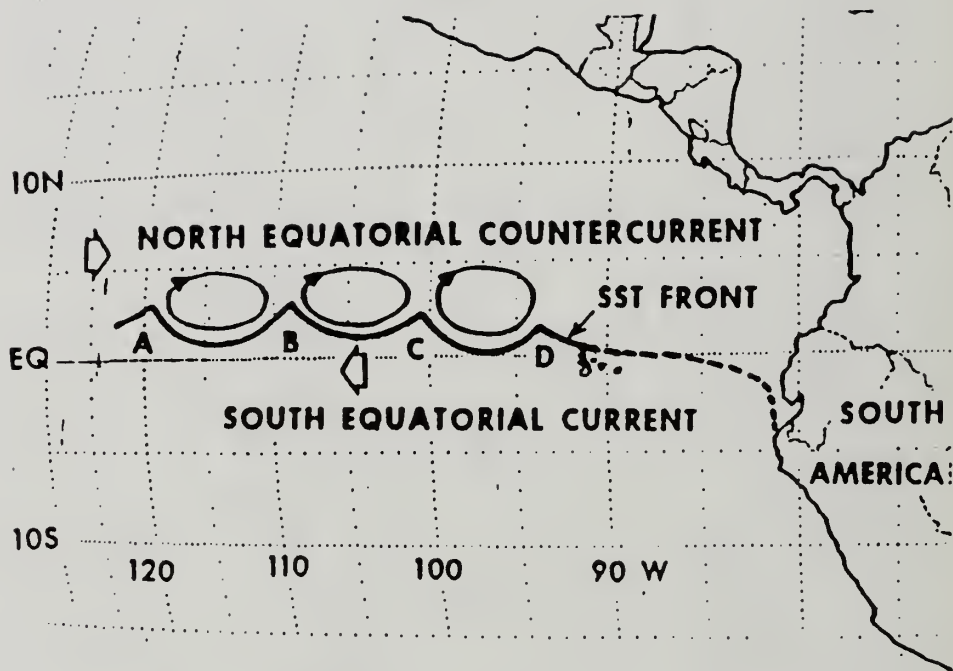


**Figure 3.3** Schematic representation of wave-like sea surface temperature front in the eastern equatorial Pacific. The anticyclonic, eddy-like patterns were inferred from drifting buoy tracks. (from Legeckis *et.al.*, 1983).

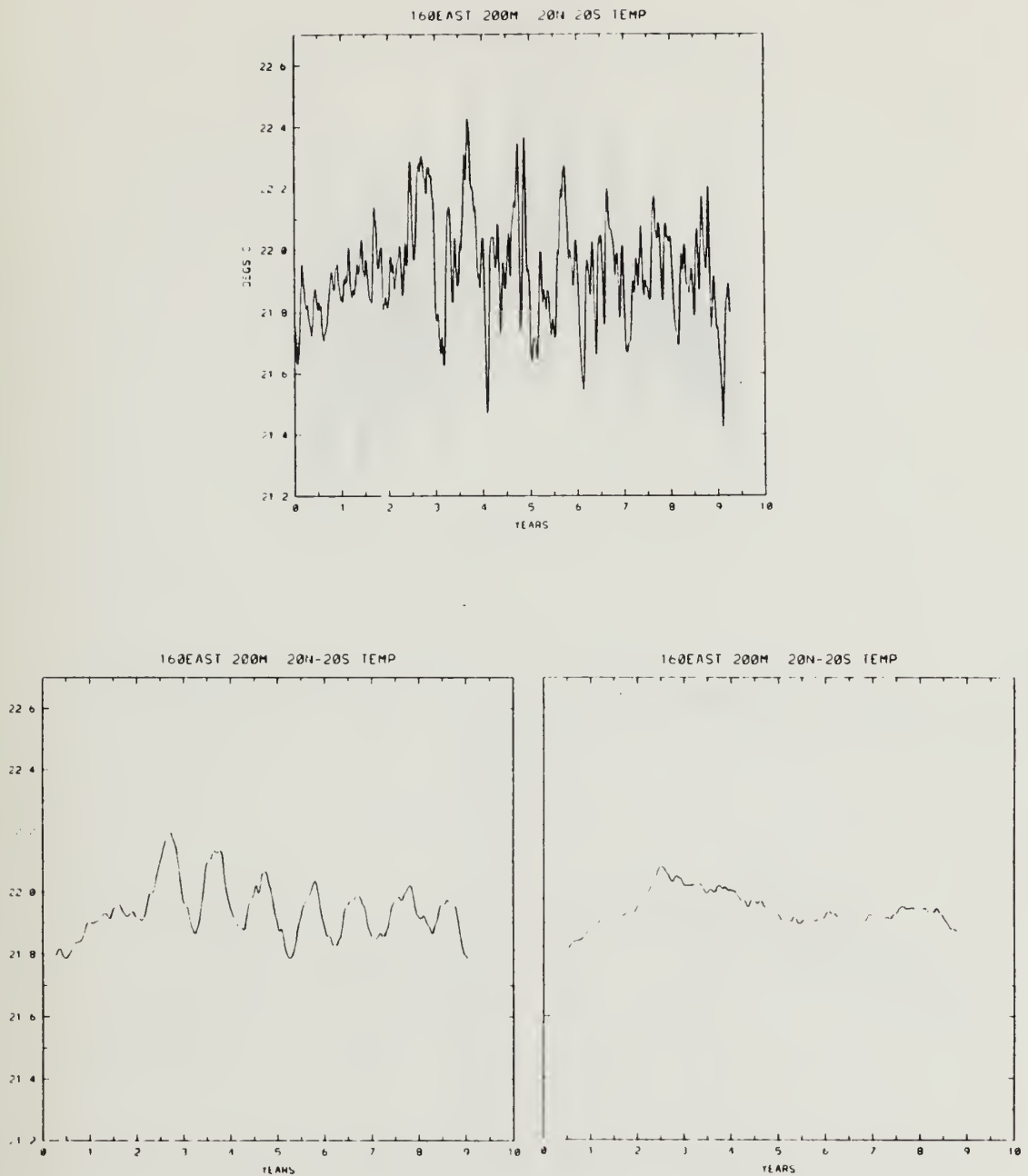


**Figure 3.4** Time series of integrated temperature along 200 m depth from 20°N-20°S at 160°E: (a) 3-day running mean, (b) 180-day running mean, and (c) 360-day running mean.



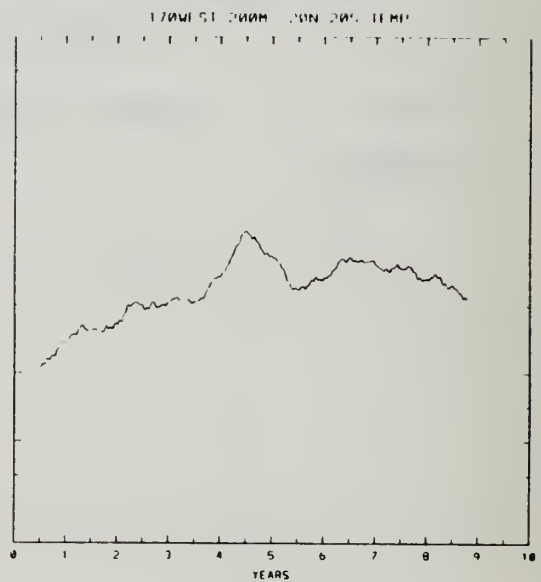
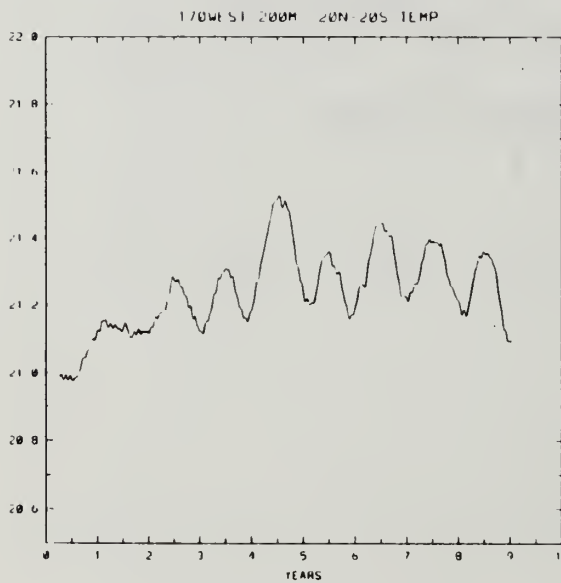
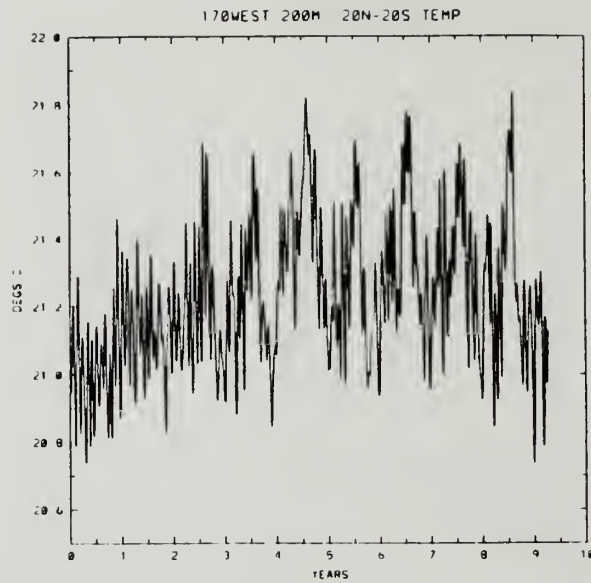


**Figure 3.5** Time series of integrated temperature along 200 m depth from 20°N-20°S at 170°W: (a) 3-day running mean, (b) 180-day running mean, and (c) 360-day running mean.

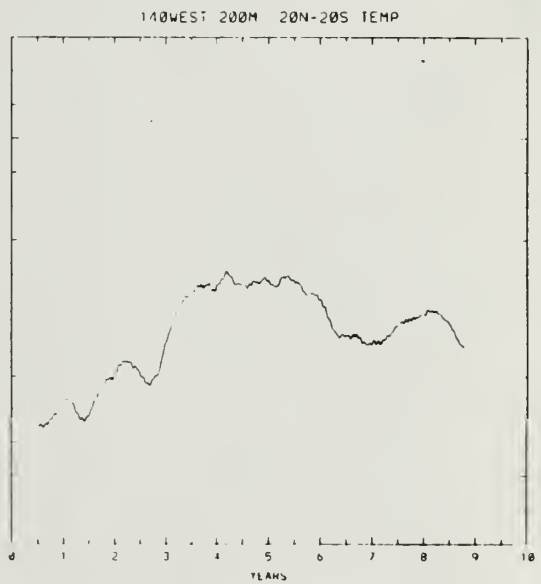
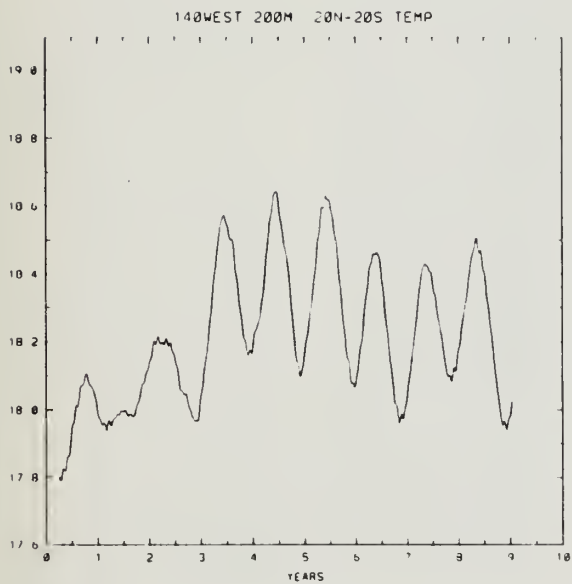
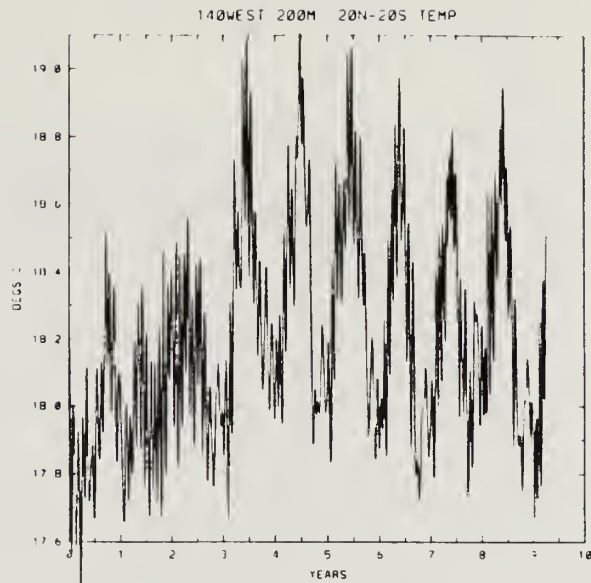


**Figure 3.6** Time series of integrated temperature along 200 m depth from 20°N-20°S at 140°W: (a) 3-day running mean, (b) 180-day running mean, and (c) 360-day running mean.

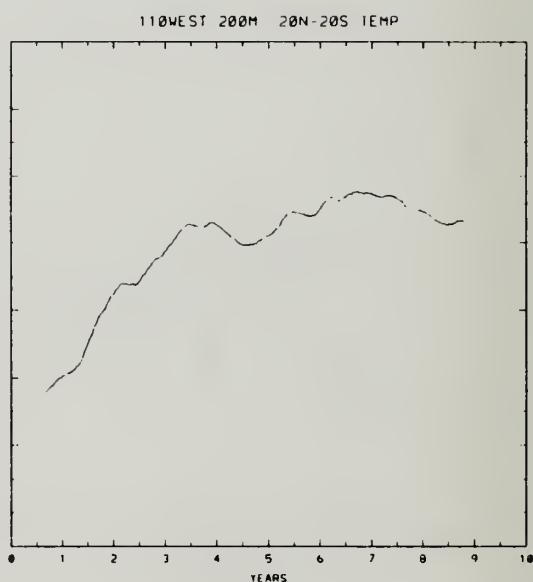
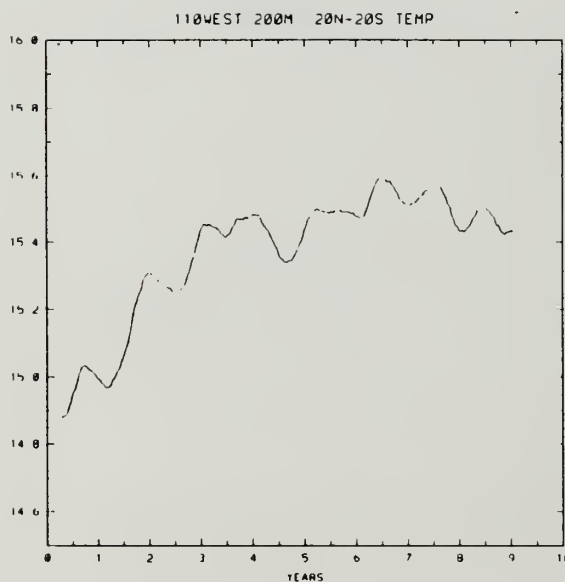
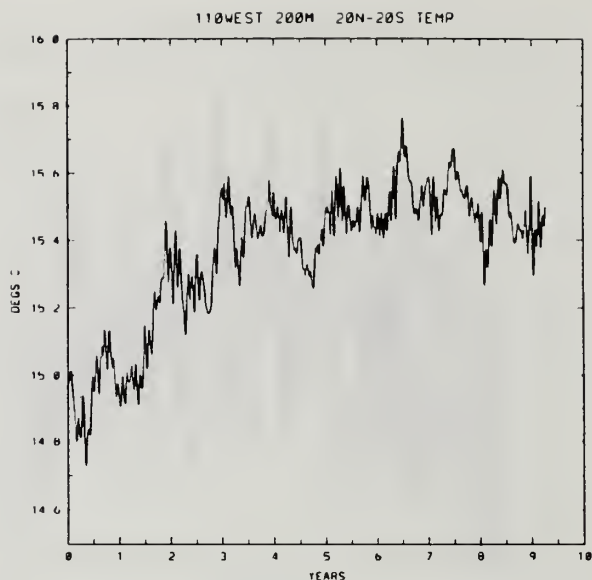


**Figure 3.7** Time series of integrated temperature along 200 m depth from 20°N-20°S at 110°W: (a) 3-day running mean, (b) 180-day running mean, and (c) 360-day running mean.

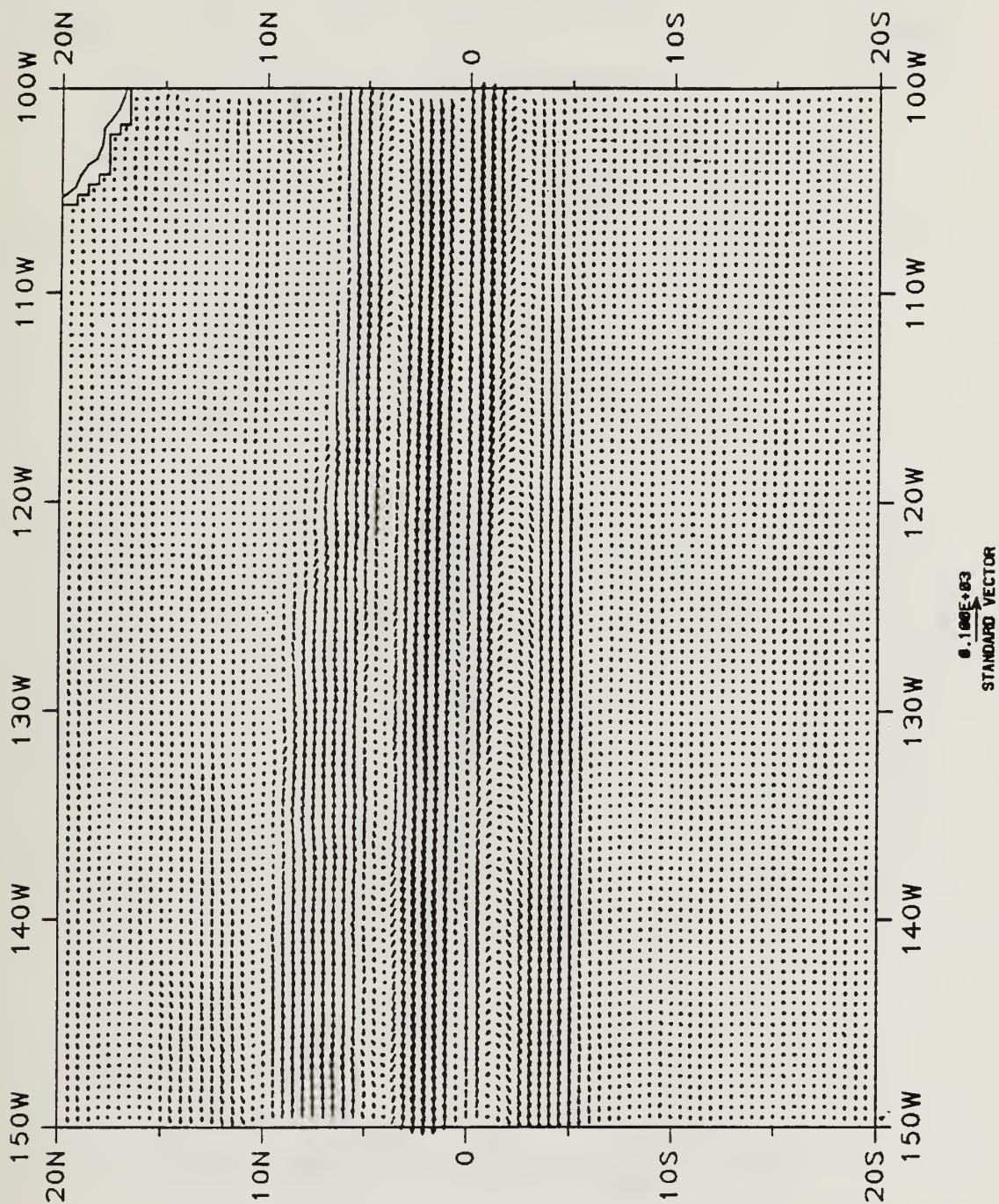


**Figure 3.8** Mean annual near surface currents (37.5 meters) in central eastern Pacific for year 4.



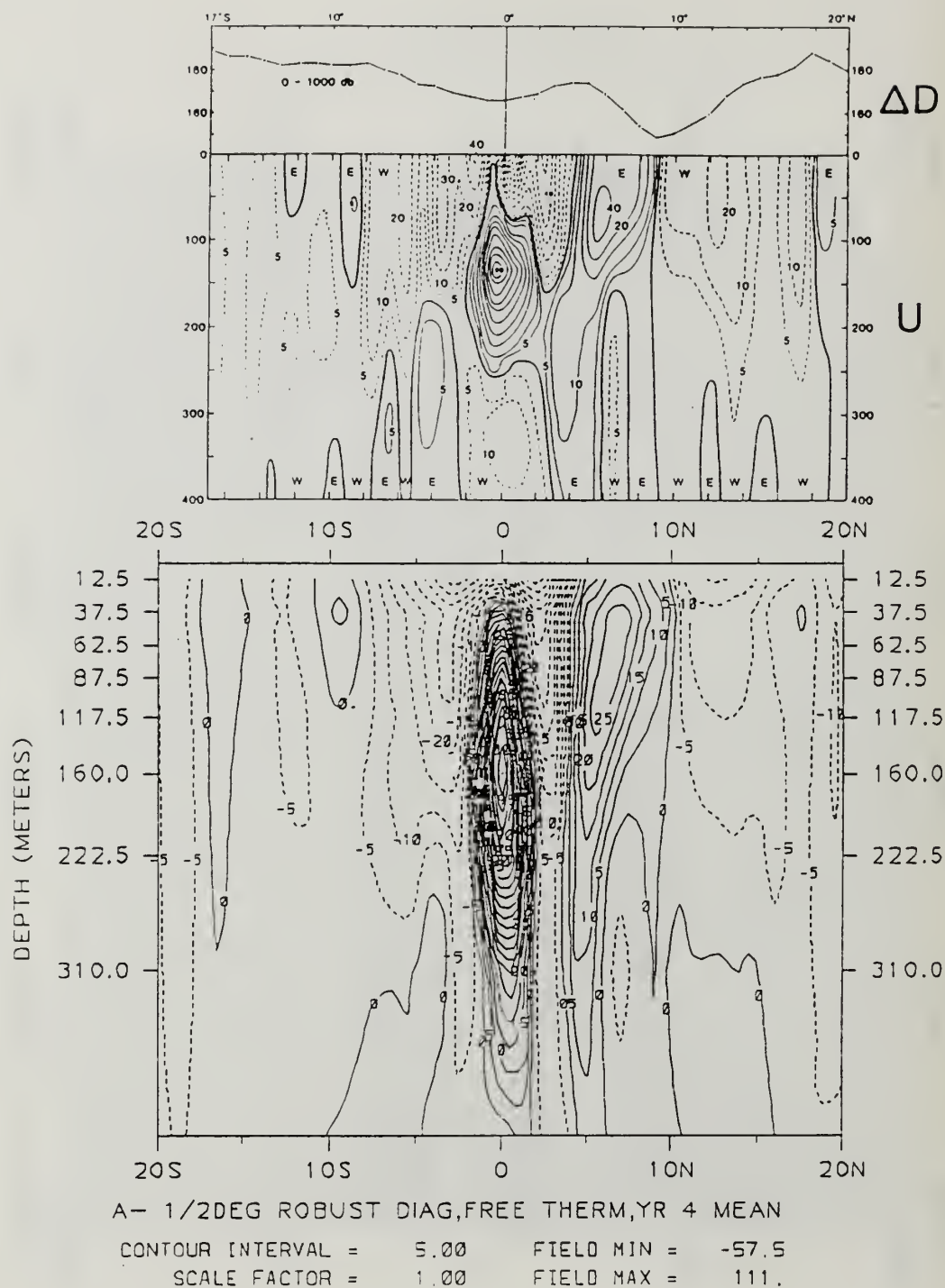


**Figure 3.9** Meridional section of mean annual zonal velocity during a) Hawaii-to-Tahiti Shuttle Experiment (from Wyrki and Kilonsky, 1984) and b) year 4 of the model. Contour interval is  $5 \text{ cm s}^{-1}$ .

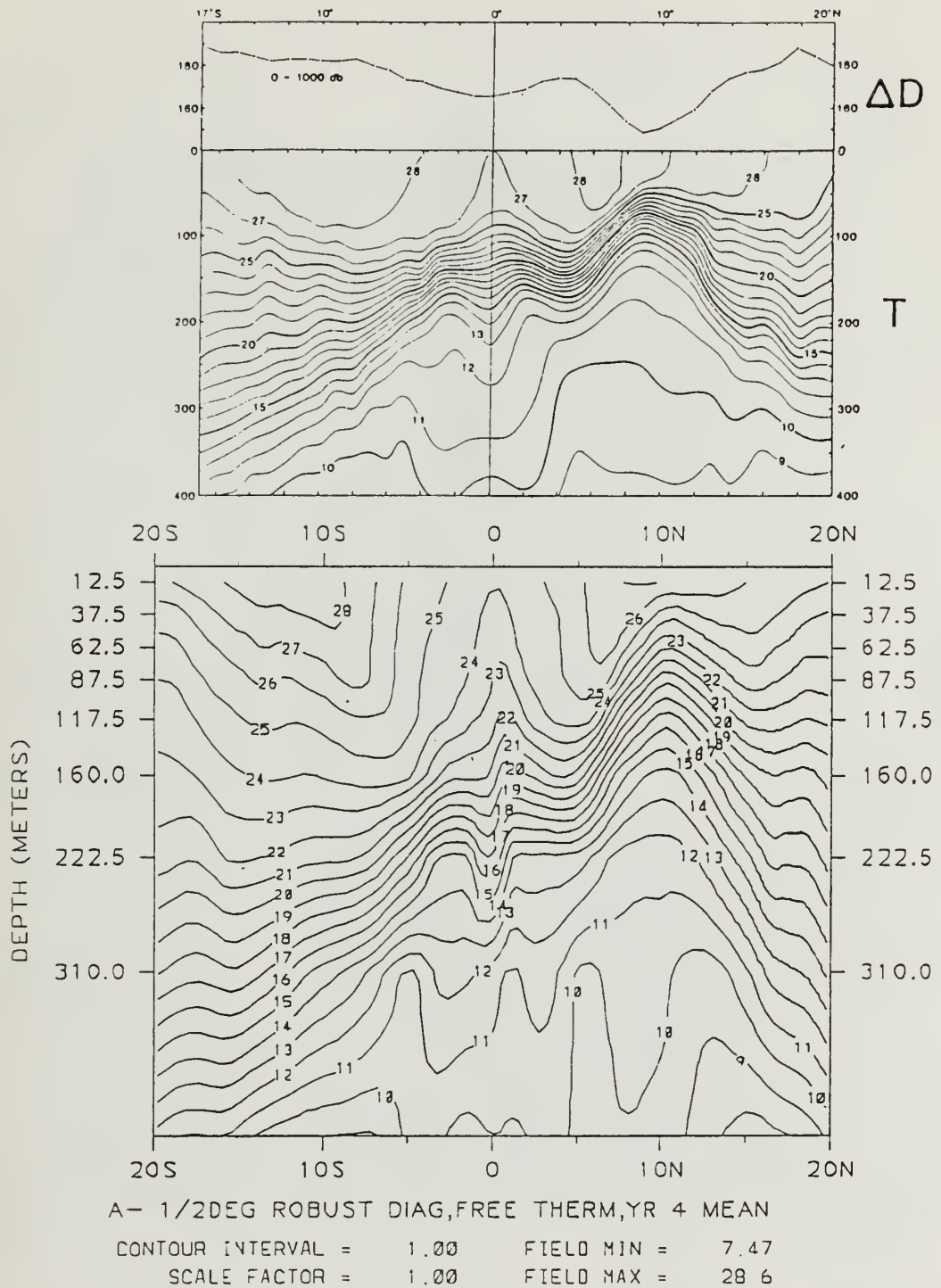


**Figure 3.10** Meridional section of mean annual temperature distribution during a) Shuttle Experiment (from Wyrski and Kilonsky, 1984) and b) year 4 of the model. Contour interval is 1°C and depth limit is 435 meters in the model figure.

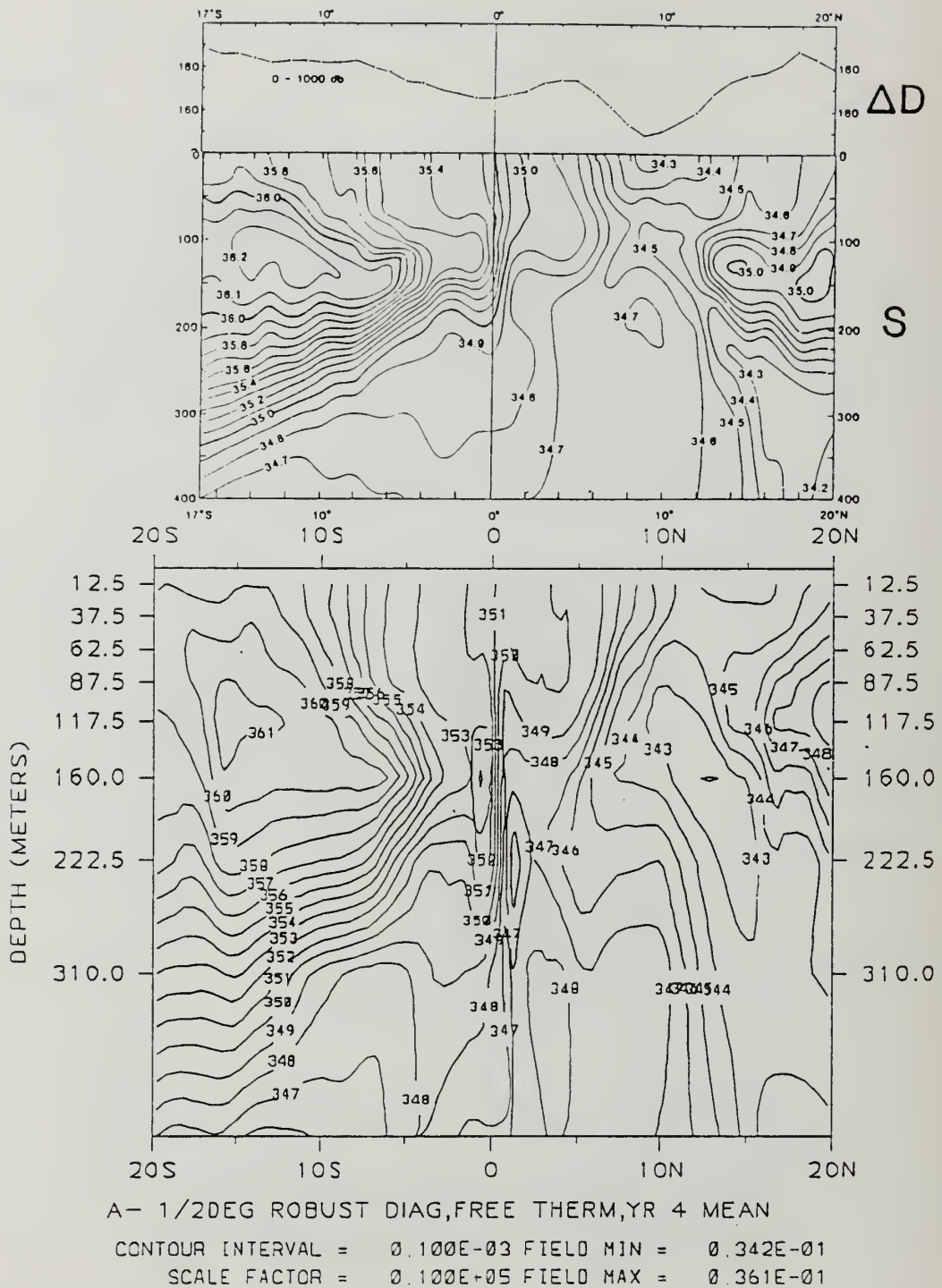


**Figure 3.11** Meridional section of mean annual salinity distribution during a) Shuttle Experiment (from Wyrski and Kilonsky, 1984) and b) year 4 of the model. Contour interval is .1 psu and depth limit is 435 meters in the model figure.

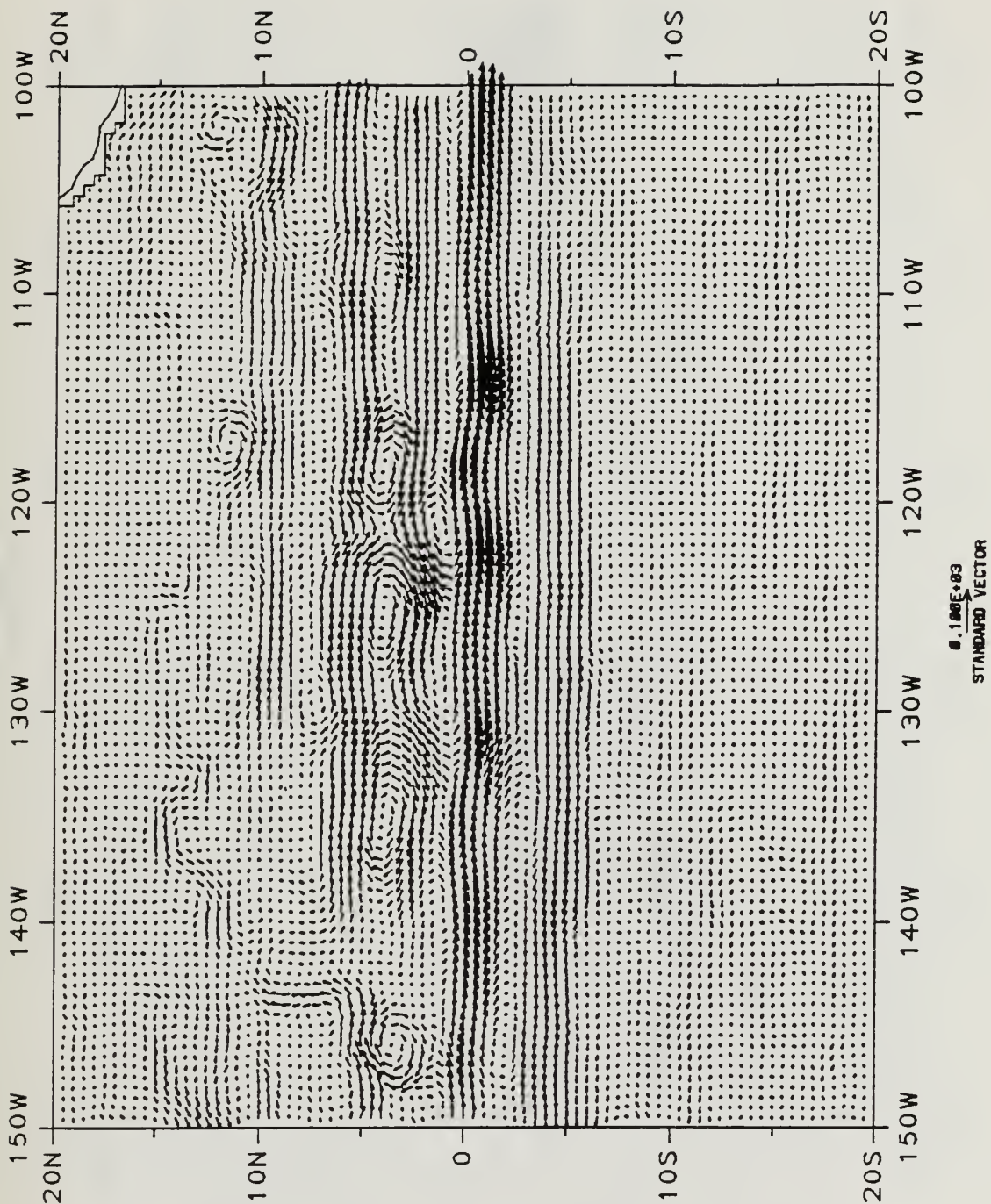


**Figure 3.12** Mean monthly current vectors for May of Year 4 in central Pacific portion of the model . Surfacing of Equatorial Undercurrent is apparent along equator. Depth depicted is 37.5 meters.



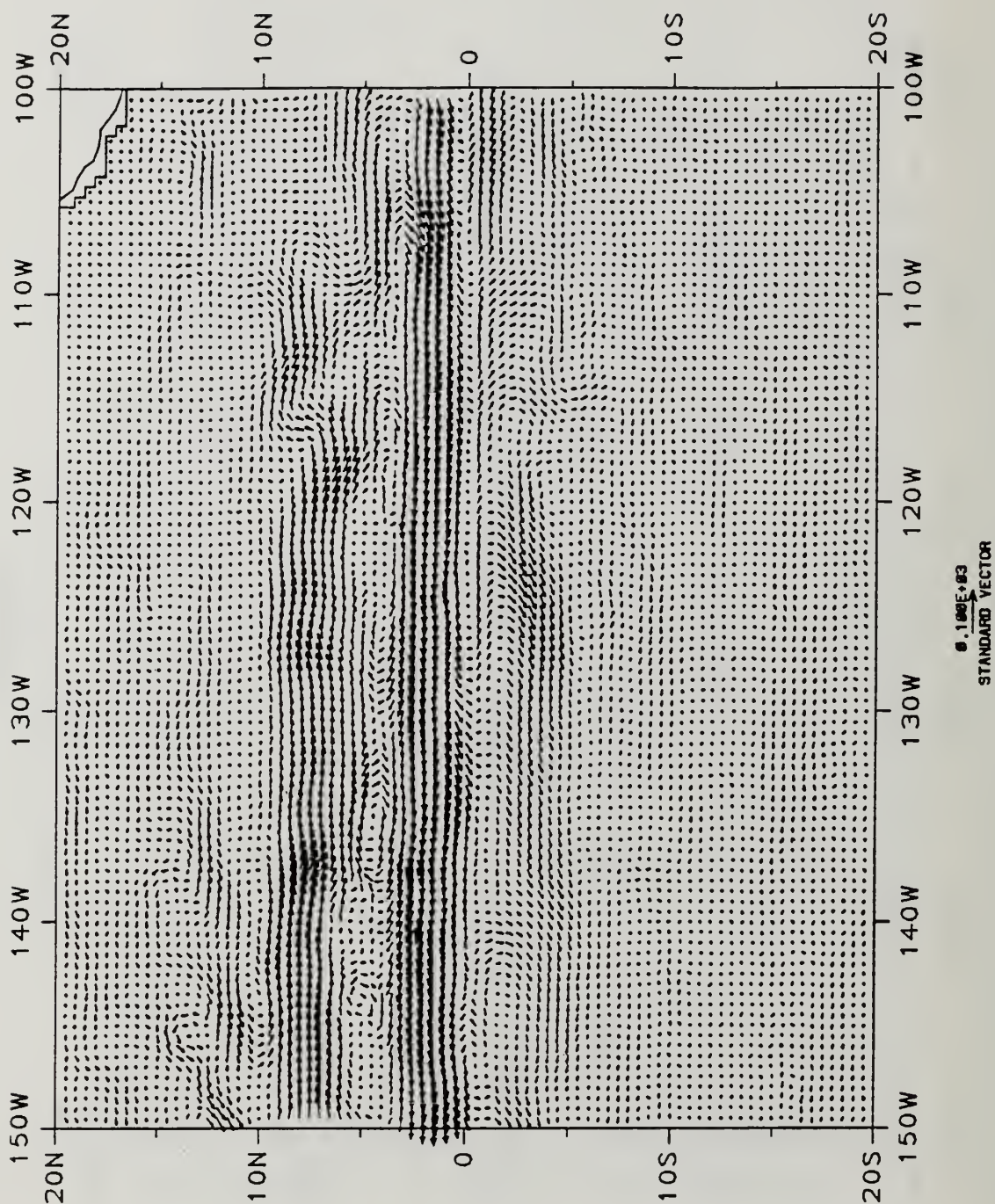
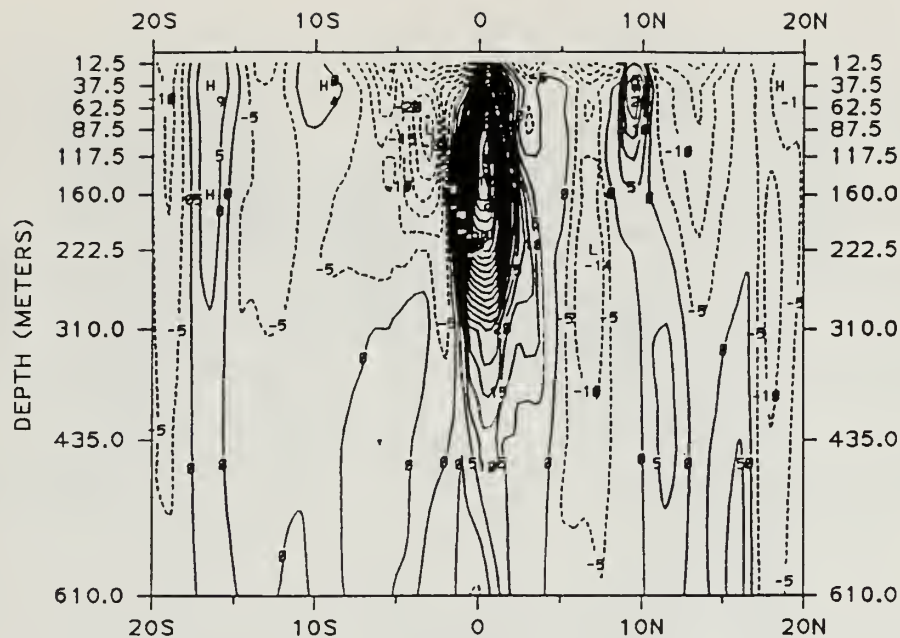
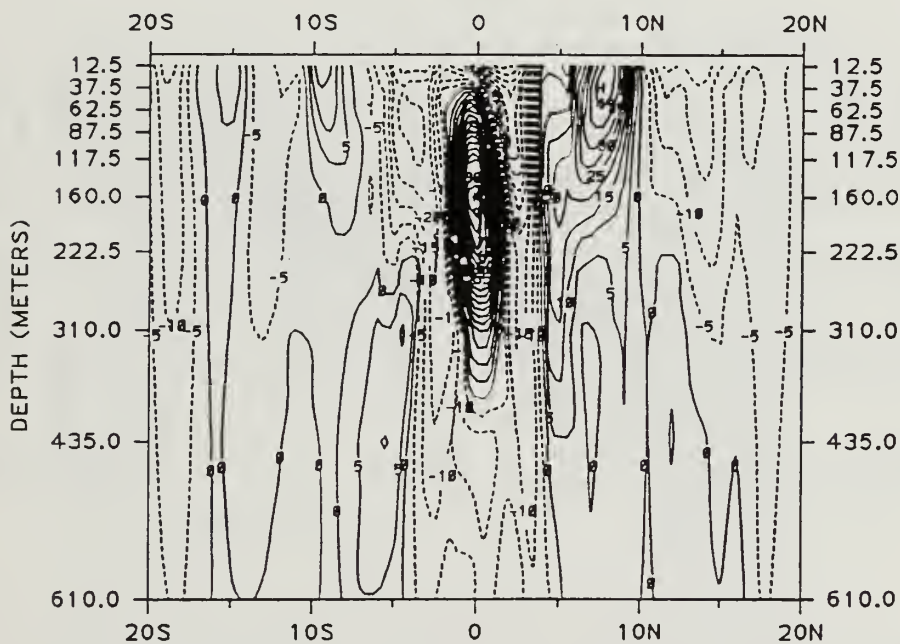


**Figure 3.13** Mean monthly current vectors for November of Year 4 in central Pacific. Equatorial Undercurrent has submerged and North Equatorial Countercurrent and South Equatorial Current are now dominant. Depth depicted is 37.5 meters.



A- SEASONALLY FORCED, MONTHLY MEAN

CONTOUR INTERVAL = 5.00      FIELD MIN = -36.0  
SCALE FACTOR = 1.00      FIELD MAX = 121.



A- SEASONALLY FORCED, MONTHLY MEAN

CONTOUR INTERVAL = 5.00      FIELD MIN = -62.1  
SCALE FACTOR = 1.00      FIELD MAX = 96.5

**Figure 3.14** Meridional section along  $160^{\circ}\text{W}$  of mean monthly zonal velocity during  
a) May of year 4 and b) November of year 4. Contour interval is  $5 \text{ cm s}^{-1}$ .

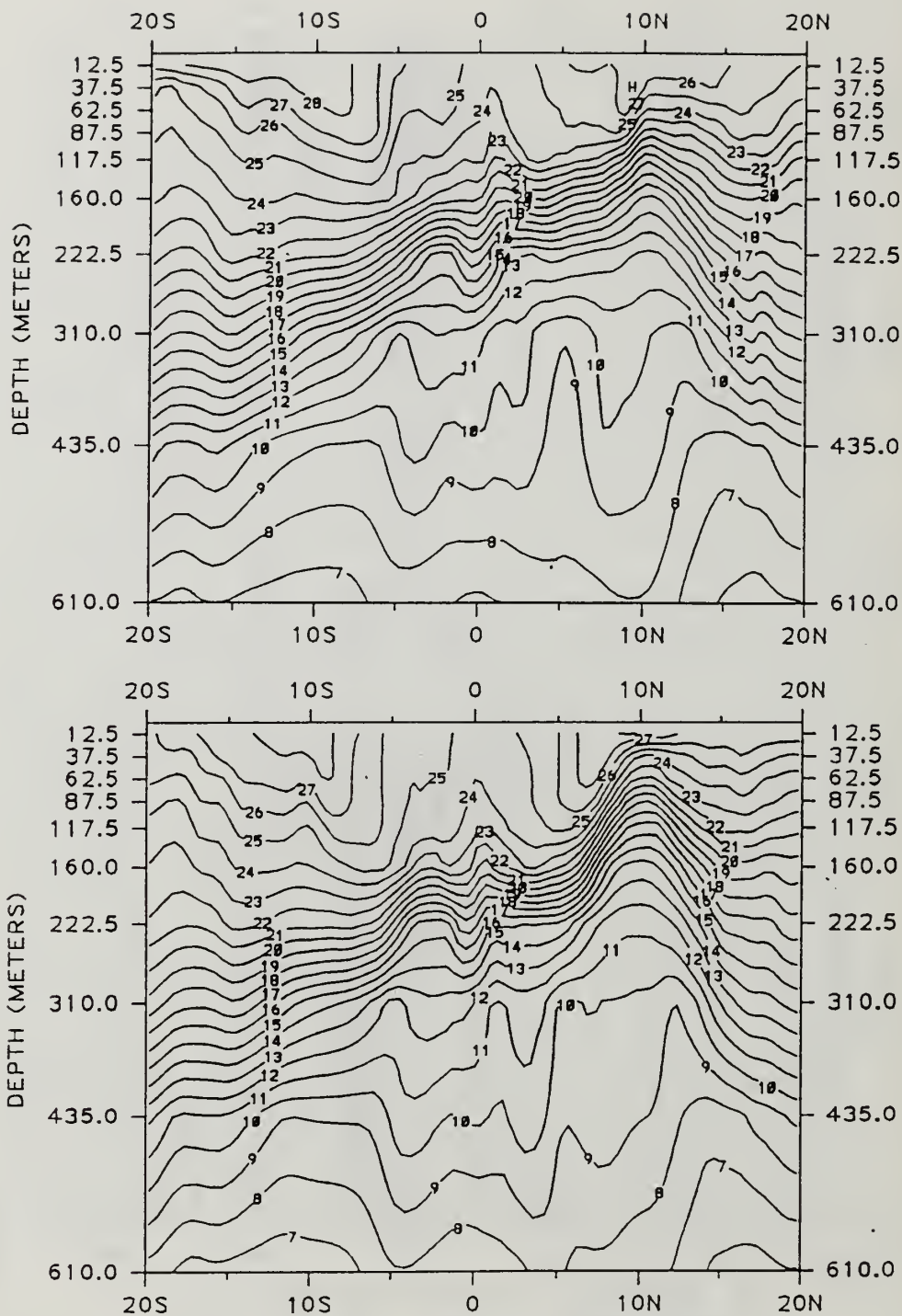


**Figure 3.15** Meridional section along 160°W of mean monthly temperature distribution during a) May of year 4 and b) November of year 4. Contour interval is 1°C.

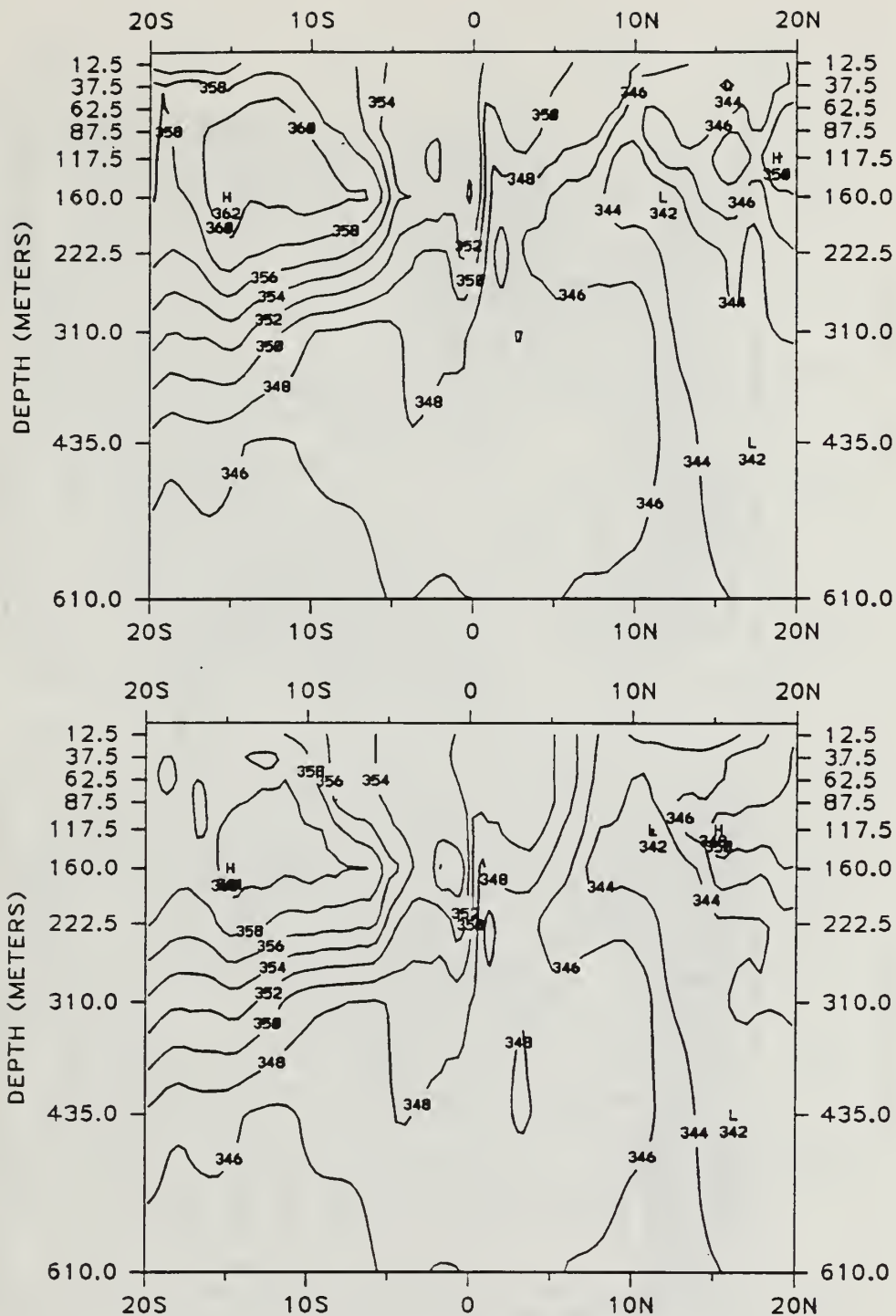


**Figure 3.16** Meridional section along 160°W of mean monthly salinity distribution during a) May and b) November of year 4. Contour interval is .2 psu.



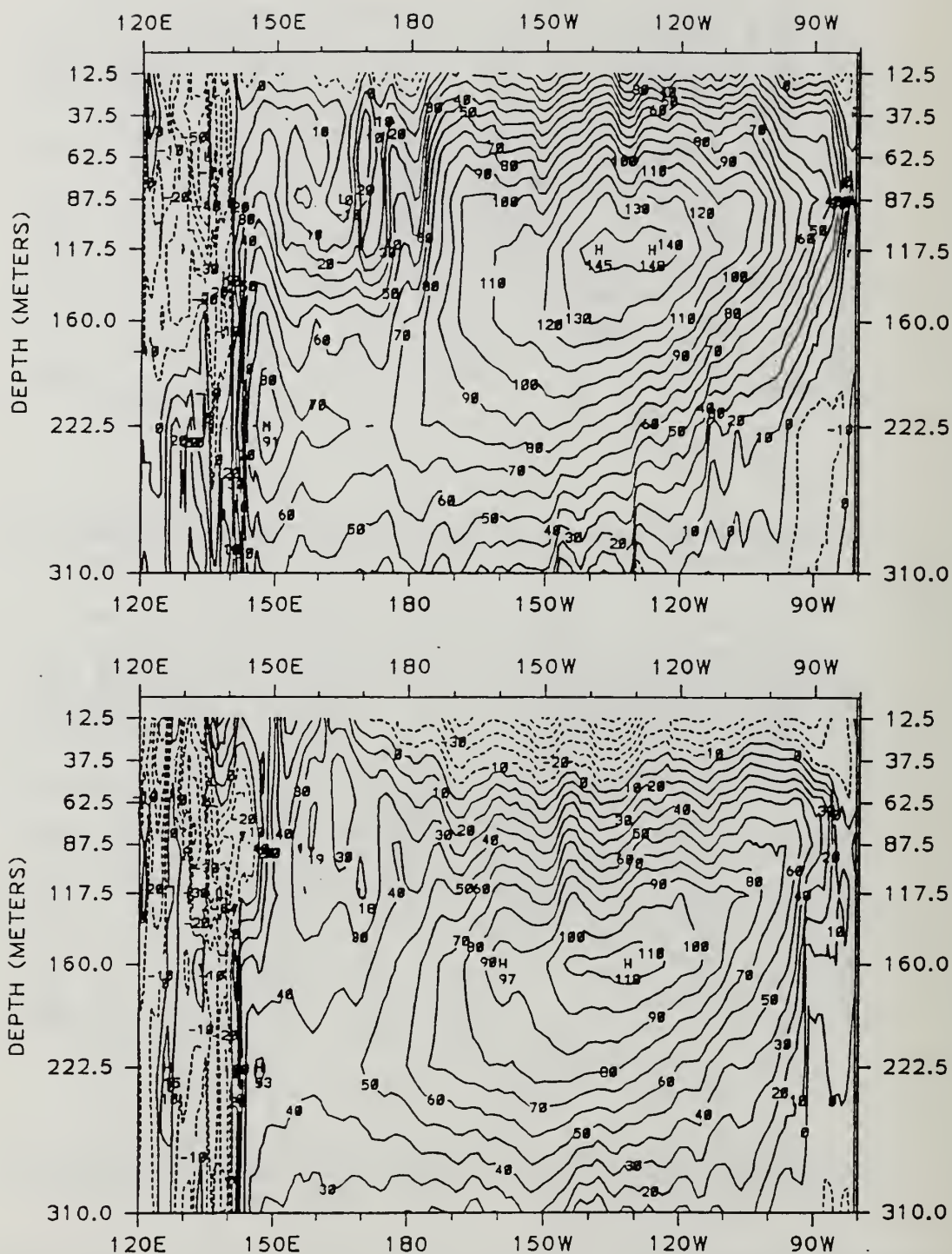


**Figure 3.17** Equatorial section of zonal velocity during a) May of year 4 and b) November of year 4. Contour interval is  $10 \text{ cm s}^{-1}$ .

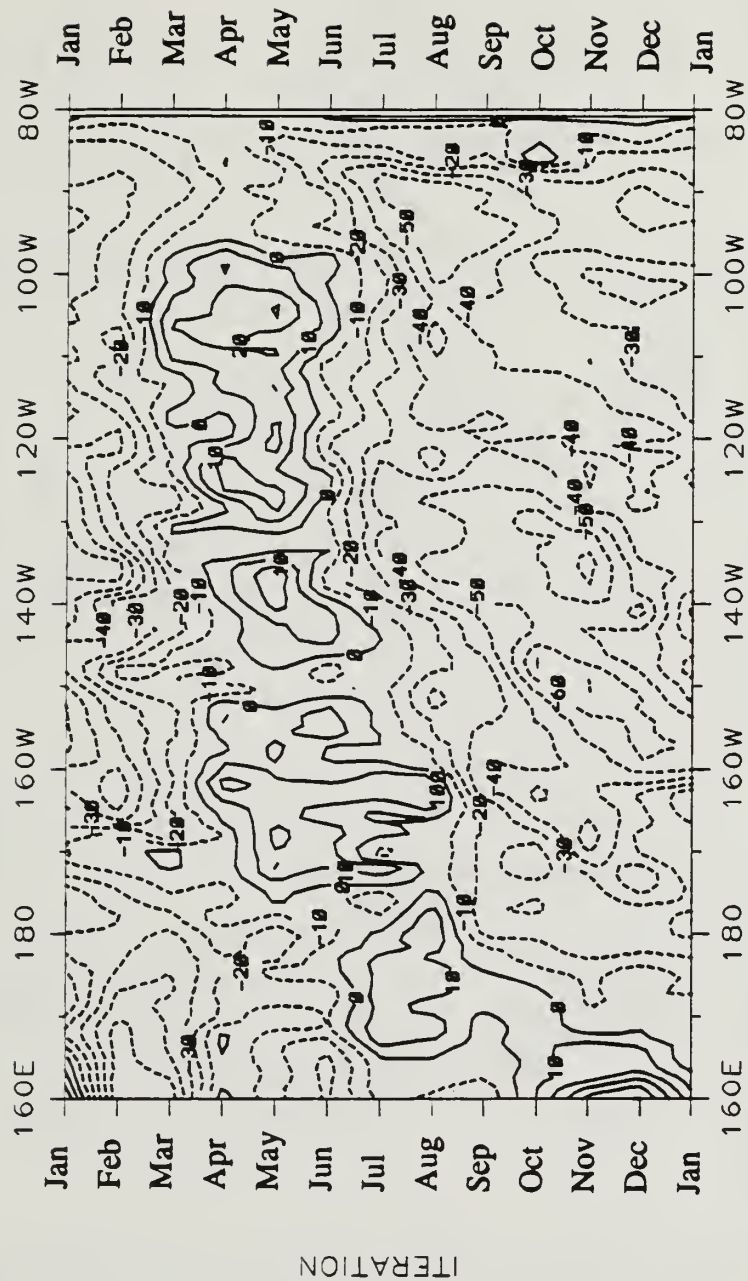


**Figure 3.18** Longitude-time plot of zonal velocity along the equator during Year 4 at 12.5 meters. Contour interval is  $10 \text{ cm s}^{-1}$ .

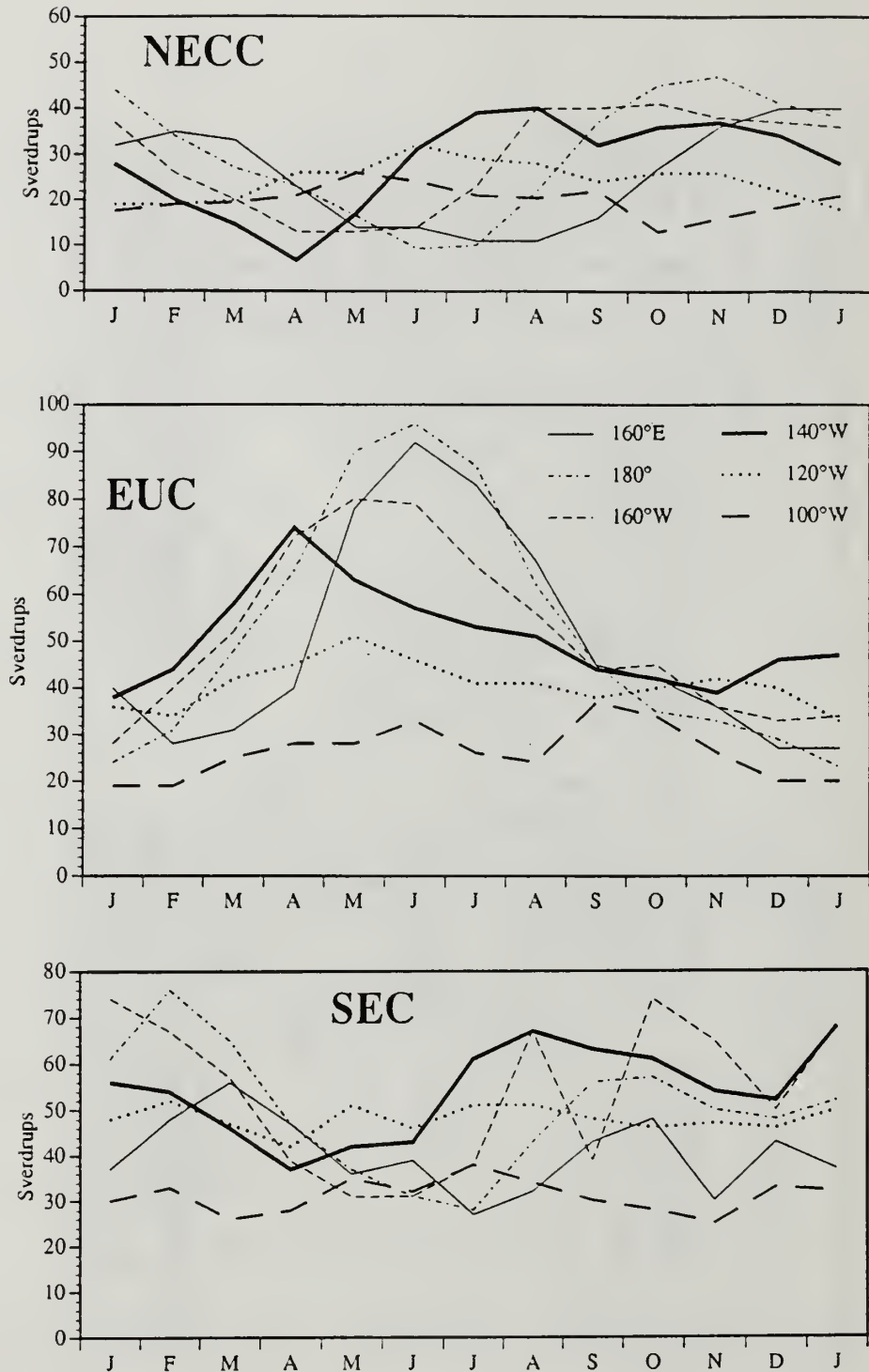


**Figure 3.19** Zonal volume transport of mean monthly equatorial currents along various meridians, a) North Equatorial Countercurrent b) Equatorial Undercurrent c) South Equatorial Current.

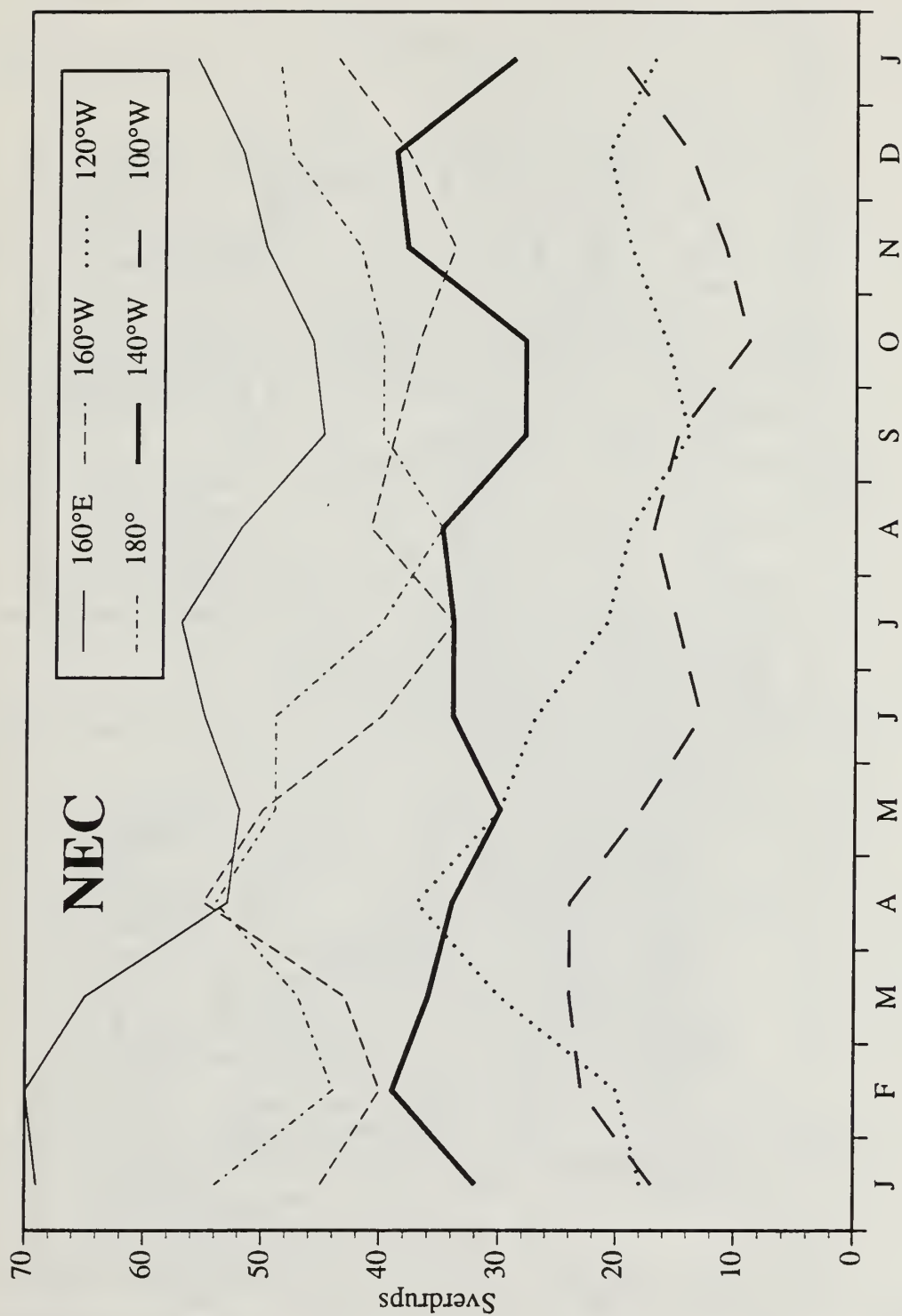
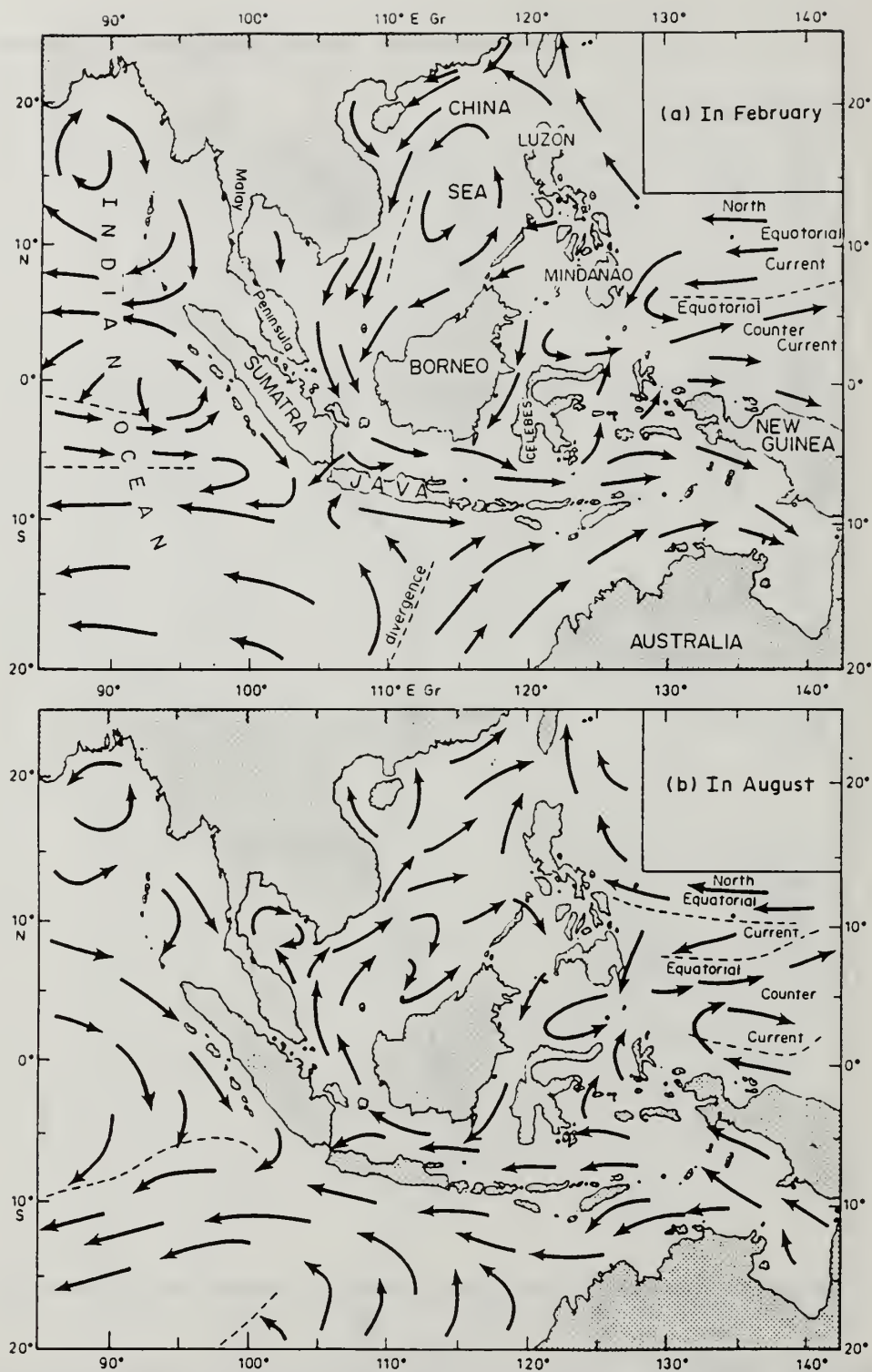
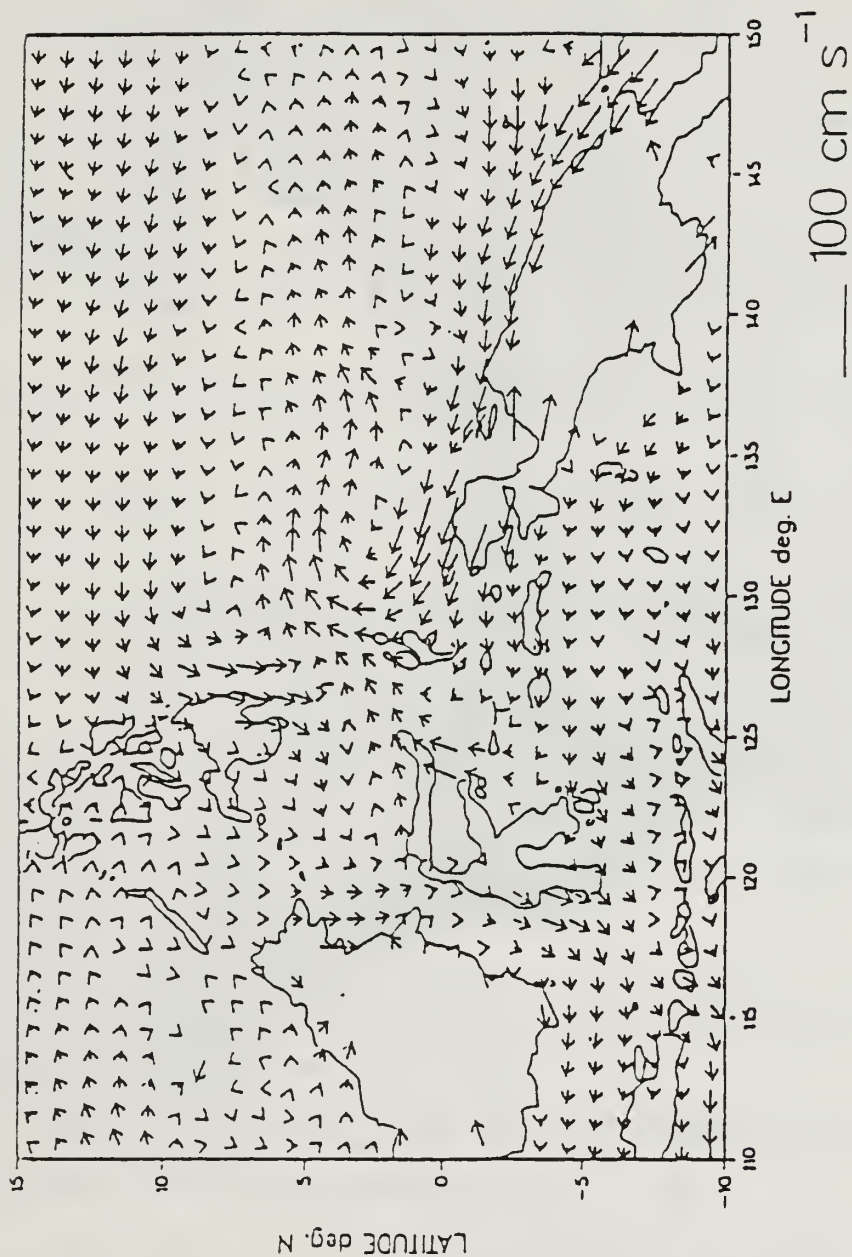


Figure 3.20 Zonal transport of North Equatorial Current in Sverdrups ( $10^6 \text{ m}^3 \text{ s}^{-1}$ ).





**Figure 3.21** Current pattern in the western Pacific during a) February and b) August. (from Tchernia, 1980).



**Figure 3.22** Historical monthly-mean ship drift observations in the western Pacific from May through November. (from Hacker, *et.al.*, 1989)

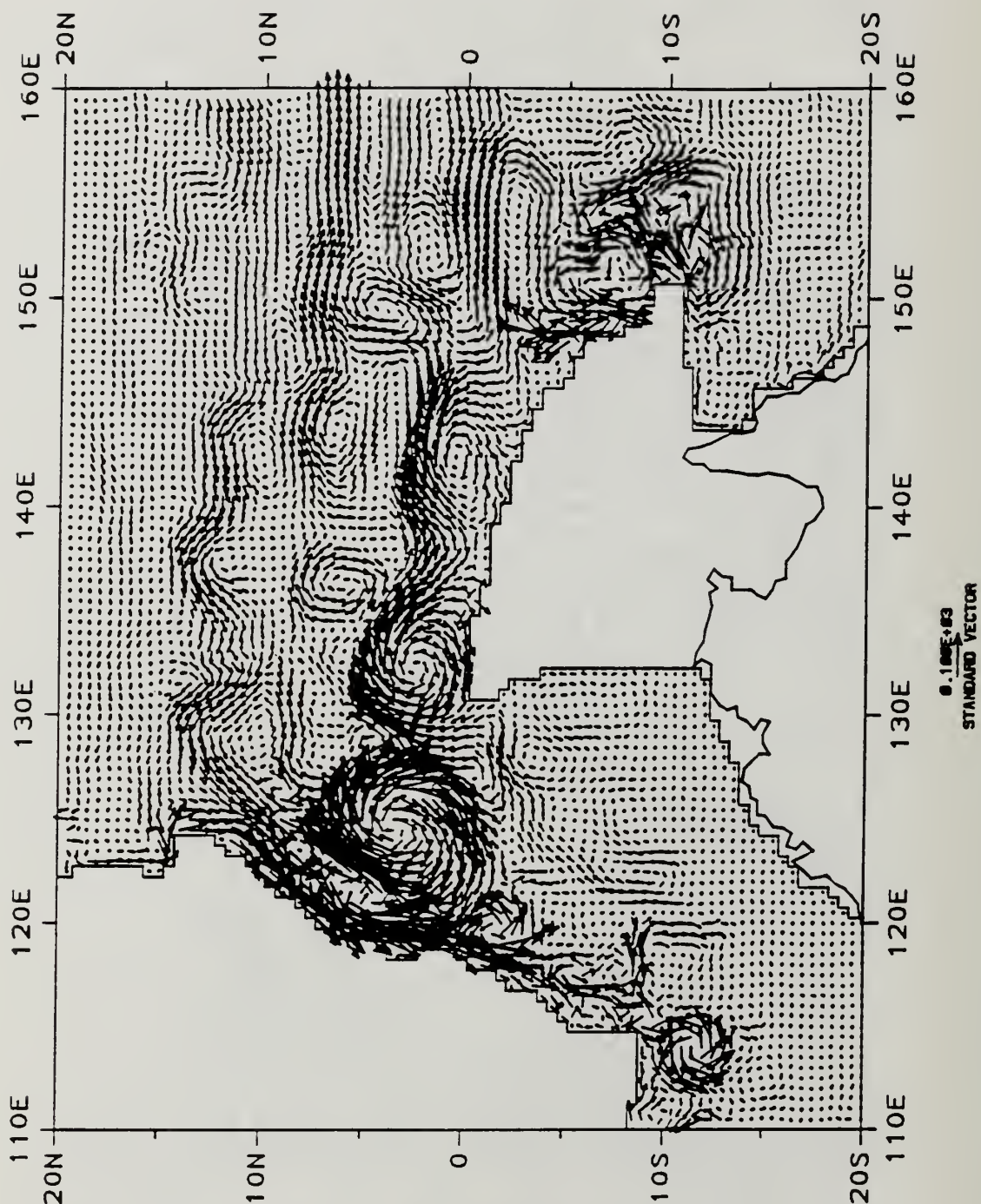


**Figure 3.23** Instantaneous current vectors in western Pacific for 14 November, year 4 of model.

## LIST OF REFERENCES

- Cox, M. D., 1980: Generation and propagation of 30-day waves in a numerical model of the Pacific. *J. Phys. Oceanogr.*, **10**, 1168-1186.
- Gill, A. E., 1982: *Atmosphere-Ocean Dynamics.*, Academic Press, Orlando, 662 pp.
- Hacker, P., E. Firing, R. Lukas, P. L. Richardson, and C. A. Collins, 1989: Observations of the low-latitude western boundary circulation in the Pacific during WEPOCS III. *Proceedings of the Western Pacific International Meeting and Workshop on TOGA COARE* (ed. J. Picaut, R. Lukas and T. Delacroix), 135-143.
- Haney, R. L., 1971: Surface thermal boundary condition for ocean circulation models. *J. Phys. Oceanogr.*, **1**, 241-248.
- Hansen, D. V., and C. A. Paul, 1984: Genesis and effects of long waves in the equatorial Pacific. *J. Geophys. Res.*, **89**, 10 431-10 440.
- Hellerman, S., and M. Rosenstein, 1983: Normal monthly wind stress over the world ocean with error estimates. *J. Phys. Oceanogr.*, **13**, 1093-1104.
- Killworth, P. D., D. J. Webb, D. Stainforth, and S. M. Paterson, 1991: The development of a free-surface Bryan-Cox-Semtner ocean model. *J. Phys. Oceanogr.*, **21**, 1333-1348.
- Legeckis, R., 1977: Long waves in the eastern equatorial Pacific Ocean: A view from a geostationary satellite. *Science*, **197**, 1179-1181.
- Legeckis, R., W. Pichel, and G. Nesterczuk, 1983: Equatorial long waves in geostationary satellite observations and in a multichannel sea surface temperature analysis. *Bull. Amer. Meteorol. Soc.*, **64**(2), 133-139.
- Levitus, S., 1982: Climatological atlas of the world oceans. NOAA Prof. Pap. 13, U.S. Government Printing Office, Washington, D. C.
- McCreary, J. P., 1987: A model of deep equatorial jets. In: *Further Progress in Equatorial Oceanography*. Eds. E. J. Katz and M. J. White, Nova University Press, 385-395.



- Pacanowski, R. C., and S. G. H. Philander, 1981: Parameterization of vertical mixing in numerical models of tropical oceans. *J. Phys. Oceanogr.*, **11**, 1443-1451.
- Philander, S. G. H., 1978: Instabilities of zonal equatorial currents. *J. Geophys. Res.*, **83**, 3697-3682.
- Philander, S. G. H., W. J. Hurlin, and A. D. Seigel, 1987: Simulation of the seasonal cycle of the tropical Pacific Ocean. *J. Phys. Oceanogr.*, **17**, 1986-2002.
- Pickard, G. L., and W. J. Emery, 1982: *Descriptive Physical Oceanography.*, Pergamon Press, Oxford, 249 pp.
- Pullen, P. E., R. L. Bernstein, and D. Halpern, 1987: Equatorial long-wave characteristics determined from satellite sea surface temperature and in situ data. *J. Geophys. Res.*, **92**, 742-748.
- Semtner, A. J., 1986a: History and methodology of modelling the circulation of the world ocean. In: *Advanced Physical Oceanographic Numerical Modelling*. Ed. J. J. O'Brien, D. Reidel, Norwell, Massachusetts, 23-32.
- Semtner, A. J., 1986b: Finite-difference formulation of a world ocean model. In: *Advanced Physical Oceanographic Numerical Modelling*. Ed. J. J. O'Brien, D. Reidel, Norwell, Massachusetts, 187-202.
- Semtner, A. J., and R. M. Chervin, 1988: A simulation of the global ocean circulation with resolved eddies. *J. Geophys. Res.*, **93**, 15502-15522.
- Semtner, A. J., and W. R. Holland, 1980: Numerical simulation of equatorial ocean circulation. Part I: A basic case in turbulent equilibrium. *J. Phys. Oceanogr.*, **10**, 667-693.
- Tchernia, P., 1980. *Descriptive Regional Oceanography*. Pergamon Press, Oxford, 253 pp., 19 plates.
- Tsuchiya, M., 1975: Subsurface countercurrents in the eastern equatorial Pacific Ocean. *J. Mar. Res.*, **33**(Suppl.), 145-175.
- Wyrtki, K., 1978: Lateral oscillations of the Pacific Equatorial Countercurrent. *J. Phys. Oceanogr.*, **8**, 530-532.
- Wyrtki, K., and B. Kilonsky, 1984: Mean water and current structure during the Hawaii-to-Tahiti Shuttle Experiment. *J. Phys. Oceanogr.*, **14**, 242-254.

## INITIAL DISTRIBUTION LIST

	No. Copies
1. Defense Technical Information Center Cameron Station Alexandria, VA 22314	2
2. Library, Code 52 Naval Postgraduate School Monterey, CA 93943-5000	2
3. Chairman (Code OC/Co) Department of Oceanography Naval Postgraduate School Monterey, CA 93943-5000	1
4. Chairman (Code MR/Hy) Department of Meteorology Naval Postgraduate School Monterey, CA 93943-5000	1
5. Professor A. J. Semtner (Code OC/Se) Department of Oceanography Naval Postgraduate School Monterey, CA 93943-5000	2
6. Professor M. L. Batteen (Code OC/Bv) Department of Oceanography Naval Postgraduate School Monterey, CA 93943-5000	1
7. Lieutenant Commander Larry Gordon PSC 819 Box 31 FPO AE, 09645-3200	1
8. Director Naval Oceanography Division Naval Observatory 34th and Massachusetts Avenue NW Washington, DC 20390	1

9. Commander 1  
Naval Oceanography Command  
Stennis Space Center  
Bay St. Louis, MS 39529-5000
10. Commanding Officer 1  
Naval Oceanographic Office  
Stennis Space Center  
Bay St. Louis, MS 39522-5001
11. Commanding Officer 1  
Fleet Numerical Oceanography Center  
Monterey, CA 93943-5005
12. Commanding Officer 1  
Naval Ocean Research and Development Laboratory  
Stennis Space Center  
Bay St. Louis, MS 39522-5004
13. Director 1  
Naval Oceanographic and Atmospheric  
Research Laboratory  
Monterey, CA 93943-5006
14. Chairman 1  
Oceanography Department  
U. S. Naval Academy  
Annapolis, MD 21402
15. Chief of Naval Research 1  
800 N. Quincy Street  
Arlington, VA 22217
16. Office of Naval Research (Code 420) 1  
Naval Ocean Research and Development Activity  
800 N. Quincy Street  
Arlington, VA 22217
17. Scientific Liaison Office 1  
Office of Naval Research  
Scripps Institution of Oceanography  
La Jolla, CA 92037

- |     |   |   |
|-----|---|---|
| 18. | Library<br>Scripps Institution of Oceanography<br>P.O. Box 2367<br>La Jolla, CA 92037   | 1 |
| 19. | Library<br>Department of Oceanography<br>University of Washington<br>Seattle, WA 98105  | 1 |
| 20. | Library<br>CICESE<br>P.O. Box 4803<br>San Ysidro, CA 92073  | 1 |
| 21. | Commander<br>Oceanographic Systems Pacific<br>Box 1390<br>Pearl Harbor, HI 96860  | 1 |
| 22. | Commander (AIR-370)<br>Naval Air Systems Command<br>Washington, DC 20360  | 1 |
| 23. | Chief, Ocean Services Division<br>National Oceanic and Atmospheric Administration<br>8060 Thirteenth Street<br>Silver Springs, MD 20910 | 1 |
| 24. | Dr. R. M. Chervin<br>Climate and Global Dynamics Division<br>National Center for Atmospheric Research<br>Boulder, CO 80307-3000         | 1 |
| 25. | Mr. Michael McCann<br>Department of Oceanography<br>Naval Postgraduate School<br>Monterey, CA 93943-5000                                | 1 |



816655











DODLEY KNOX LIBRARY  
NAVAL POSTGRADUATE SCHOOL  
MONTEREY CA 93943-5101



GAYLORD S



DUDLEY KNOX LIBRARY



3 2768 00018942 7